Chapter 14
Compact Photonic SOI Sensors

**Souvik Ghosh, Tuffail Dar, Charusluk Viphavakit,
Chao Pan, N. Kejalakshmy and B. M. A. Rahman**

Abstract Besides well matured optical fiber-based sensors, emerging compact down-scaled nanowires, slot waveguides and resonators are now under researcher's consideration due to their high sensitivities and on-chip fabrication possibilities. Along with pure dielectric based waveguides and resonators, clever engineering of sub-wavelength field confinement and modal propagation loss in plasmonic nanowire and hybrid plasmonic slot waveguides also showing promising results in the field of photonic sensing. Numerically efficient, versatile finite element method based approaches are used for rigorous analyses, design, and optimizations of these complex optical guided-wave structures. All these sensor devices can exploit the well-developed state-of-the-art fabrication technologies.

Keywords Optical sensors · Biosensors · Silicon photonics
Finite element method

14.1 Introduction

The maturity of photonic technology not only enlighten the telecommunication industries through its high-speed data transmission but also shows a great potential in many diverse fields of applications. One of the key application has been in optical sensing. Each year, billions of dollars are invested in research and development of accurate and non-hazardous sensing technologies. All these demands impose a considerable amount of responsibility on scientists and researchers. These increased legislative requirements drive us for the innovation and development of integrated, compact, nano dimensioned photonic devices for sensing. Our focus here to present the accurate computational approaches needed for design and optimization of compact integrated photonic sensors.

S. Ghosh · T. Dar · C. Viphavakit · C. Pan · N. Kejalakshmy · B. M. A. Rahman (✉)
School of Mathematics, Computer Science, and Engineering, City University of London,
Clerkenwell EC1V 0HB, UK
e-mail: b.m.a.rahman@city.ac.uk

M. F. O. Hameed and S. Obayya (eds.), *Computational
Photonic Sensors*, https://doi.org/10.1007/978-3-319-76556-3_14

The broadened applications of photonics show a great potential in sensing applications for accurate measurement of chemical, physical and biological parameters, such as humidity, temperature, a range of selective gases, stress, strain, pressure, displacements, surface roughness, microscopic living substance, DNA hybridizations etc. Photonic sensors can easily be designed with pure dielectric materials or noble metals which make those reliable in hazardous conditions where other conventional sensors are unsafe due to fire, electrical short-circuit, high temperature, corrosive environment, and radiation risk and high electromagnetic interferences. On the other hand, for medical and bio-chemical sensing with lower weight, compact size with high precision sensitivity is highly desirable. Dielectric material and noble metal-based optical waveguides and resonators would serve those purposes for both invasive and non-invasive cases due to a much greater efficiency for detection of small refractometric changes and nano footprint. Although, fiber optic sensors are well-developed and most commercially available sensors are fiber based, the advancement in fabrication technology leads researchers to consider innovative high index contrast and composite material based sensor designs.

The design of a new system often includes individual component assessment and its effectiveness for the specially required purpose. Analytical, semi-analytical and numerical modeling of the devices are often considered to achieve an accurate and optimized design for evaluation of potential performance and unfavorable features of the device. Thus, advanced photonics modelings are helpful to predict and understand the complex sensor characteristics before expensive production and experimental validation. A complete sensing device comprises of many distributed complex optical components and waveguides. Understanding of exact fundamental physics of light guidance and wave propagation characteristics through optical components are necessary for their effective use. Several modeling methods have already been proposed based on analytical and semi-analytical approaches. A pure analytical and semi-analytical method exhibits its inability or inefficiency for the solution of practical waveguides where optical power confined in the transverse plane. Analytical approach only can solve the planar waveguide by analyzing the transcendental equations by taking field continuity at the material interfaces. In the years of 1969 and 1970 Maracatili [1], Goell [2] and Knox and Toulios [3] have introduced semi-analytical methods which can only provide solutions for simple waveguides. However, these methods also inadequate for the analyses of complex waveguide geometries containing inhomogeneous and anisotropic materials. Over last 40 years, several methods have been developed such as the matrix methods [4], the mode matching method [5], the finite difference method [6], the method of lines [7] and the spectral index method [8]. Beside these approximated approaches the full-vectorial finite element method (FV-FEM) shows its high efficiency for design and optimizations of complex structured waveguides and resonators [9–12]. Any arbitrarily shaped waveguide geometry with isotropic and anisotropic multilayered materials can easily be handled by this powerful numerical tool. Simple mathematical formulations and clever use of memory management algorithm for sparse matrices can make this method suitable for readily available computer workstations.

14.2 Integrated Slot Waveguide for Sensing

Optical waveguides initially developed for the advancement of the telecommunications. However, their efficient light-matter interactions, noise immunity, precise detection and dedicated flexible geometry make them suitable for sensing applications. Nowadays, circularly symmetric optical waveguide i.e. optical fibers are widely used for label-free macro, micro, and even nano-scale detections. Different fiber modulation designs, such as clad polishing for high evanescent light-matter interactions, intrinsic and extrinsic fiber interferometry arrangements, fiber Bragg gratings (FBG) and luminescent-based sensors could be used to dealing with specific sensing problem. Developments and applications of the fiber-based sensor are discussed in [13, 14]. But the fiber designs and productions are still limited to telecommunication applications. Thus, compared to the fiber optic sensors, the nano-dimensioned, high index contrast rib, channel, hollow-core and slot waveguides have attracted the considerable attentions in sensing based applications. Both the labeling-based and label-free sensing processes can be exploited by these exotic waveguide designs. They can be fabricated with standard lithographic techniques which results in low-cost mass production on a single-chip. Additionally, SOI based high index contrast waveguiding incorporates sensor integration with other electronic and optical components on the same chip. The rib, channel, and strip waveguides confines the lightwave in the high index core surrounded by low index medium. Here, the light guiding is based on the total internal reflection (TIR) and only a modest fraction of evanescent light tail interacts with the surrounded sensing analytes. Another interesting structure, the dielectric coated metallic hollow-core waveguide, reported by Saito et al. [15] is advantageous for biochemical liquid and gas sensing due to its light guiding mechanism through a low index core medium. It works as an absorption cell and its performance is highly wavelength dependent. However, length of this waveguide is much larger (few meters) compared to the integrated waveguides (few microns). On the other hand, the integrated slot waveguide has a unique light guiding mechanism that confines light in a low index slot. This nanometer wide gap/slot is formed in between two high index dielectrics, dielectric-metal or metal-metal strips. Thus, the electric field normal to the high and low index interface becomes discontinuous. Depending upon the slot orientations, the waveguide could be either vertical, horizontal or a combination of both, forming a cross-slot. In case of both vertical and horizontal slot waveguides, the dominant electric field components (E_x and E_y) of the quasi-TE and TM mode, respectively, encounters discontinuities at the material interfaces. Thus, instead of an evanescent field i.e. a small fraction of the guided field for conventional waveguides, a large field enhancement has been observed for a dielectric and metal-dielectric based slot waveguides. An intense power density in the slot results in a strong light-matter interaction that makes this structure more attractive for extensive label-based, label-free and opto-mechanical sensing applications. The detection of analyte refractometric change is a major sensing mechanism for integrated optical sensors. According to problem demand, the distinct waveguide can be designed and incorporated into suitable transducer devices, such as interferometers

Table 14.1 An overview of the dielectric and hybrid plasmonic slot waveguide based photonic sensors

Sensor type	Operating wavelength	Target element	Sensitivity (*S*) and/or detection limit (*DL*)	Evaluation method	References
$Si_3N_4 - SiO_2$ based micro ring resonator	~1.3 µm	DI H_2O-ethanol solution, RI: 1.33–1.42	$S = 212$ nm/RIU $DL = 2 \times 10^{-4}$ RIU	Experimental	[16]
$Si_3N_4 - SiO_2$ based micro ring resonator	~1.3 µm	Label-free sensing: BSA and anti-BSA	BSA $S = 3.2$ nm/(ng/mm^2), DL =16 pg/mm^2 Anti-BSA $S = 1.8$ nm/(ng/mm^2), $DL = 28$ pg/mm^2	Experimental	[17]
Coupled slot SOI waveguides	1.55 µm	Glucose/water solution	0.1 g/L 10^{-5} RIU	Theory and simulations	[18]
Three SOI coupled slot waveguides	1.55 µm	Glucose/water solution ethanol/DI water solution	$S = -172$ RIU^{-1} (glucose/water) $S = 155$ RIU^{-1} (ethanol/water)	Theory and simulation	[19]
SOI based slot waveguide	1.55 µm	Bulk sensing: RI: 1.333–1.335 Surface sensing: Bio-layer, RI: 1.45	Waveguide sensitivities[a]	Simulations	[20]
Si_3N_4–SiO_2 based triple slot waveguide	1.3 µm	Bulk sensing: RI: 1.45–1.46	20% greater waveguide sensitivity than single slot[a]	Simulations and experiments	[21]
Si_3N_4 slot waveguide ring resonator	~1.55 µm	Bulk sensing: DI H_2O–NaCl solution Surface sensing: bilayer (ploy-sodium-4-styrenesulfonate/ poly-allylamine hydrochloride)	Bulk sensing: $S = 1730$ (2π)/RIU and $DL = 1.29 \times 10^{-5}$ RIU Surface sensing: $S =$ 60 nm/(ngmm^{-2}) and $DL = 0.155$ pgmm^{-2}	Simulations and experiments	[22]

(continued)

Table 14.1 (continued)

Sensor type	Operating wavelength	Target element	Sensitivity (S) and/or detection limit (DL)	Evaluation method	References
Si single and double slot microrings	~1.55 μm	Bulk sensing: water	Waveguide sensitivity[a]	Simulations	[23]
Si multiple slot based ring resonator	~1.55 μm	Water solution	$S = 912$ nm/RIU	Simulations	[24]
SOI vertical slot ring resonator	~1.55 μm	Bulk sensing: NaCl/water solution	$S = 298$ nm/RIU $DL = 4.2 \times 10^{-5}$ RIU	Simulations and experiments	[25]
Loop mirror based slot waveguide	~1.55 μm	Bulk sensing: air, water	$S = 6 \times 10^{3}$ nm/RIU	Simulations	[26]
Si_3N_4 slot based Mach-Zehnder interferometer (MZI)	~1.55 μm	Bulk sensing: streptavidin solution	$S = 1864\ \pi$/RIU $DL = 1$ pg/ml	Simulations and experiments	[27]
Grating assisted Si_3N_4 strip and slot waveguide coupler	~1.55 μm	Bulk sensing: water solution	$S = 10^{5}$ nm/RIU	Simulations	[28]
Au based plasmonic vertical slot cavity	~1.55 μm	Bulk sensing: water, acetone	$S = 600$ nm/RIU	Simulations	[29]
Double slot hybrid plasmonic MZI	~1.55 μm	Bulk sensing: isopropanol solution	$S = 1061$ nm/RIU	Simulations and experiments	[30]
Double slot plasmonic ring resonator	~1.55 μm	Bulk sensing: isopropanol	$S = 687.5$ nm/RIU $DL = 5.37 \times 10^{-6}$ RIU	Simulations and experiments	[31]
SOI based suspended slot waveguide	2.25 μm	Bulk sensing	Waveguide sensitivity = 1.123	Simulations and experiments	[32]

(continued)

Table 14.1 (continued)

Sensor type	Operating wavelength	Target element	Sensitivity (*S*) and/or detection limit (*DL*)	Evaluation method	References
Au/Si hybrid plasmonic miroing resonator	~1.55 μm	Bulk sensing: water solution	S = 580 nm/RIU	Simulations	[33]
SOI slot with sidewall Bragg gratings	~1.55 μm	Bulk sensing: multi-analyte	S = 291.93 nm/RIU $DL = 10^{-6}$ RIU	Simulations	[34]
SOI micro ring resonator	Near-IR	Acetylene gas	490 nm/RIU 10^{-4} RIU	Simulation and experiment	[35]
Silicon-on-nitride (SON) vertical slot waveguide	Mid-IR	NH_3 gas	DL = 5 ppm	Simulations	[36]
Si rib slot waveguide	Mid-IR	Gases: N_2O, CO and CH_4	DL = 0.2 ppm (N_2O) DL = 0.44 ppm (CO) DL = 36 ppm (CH_4)	Simulations	[37]

[a] A specific waveguide sensitivity is not mentioned in the report. Depending on the design parameters the waveguide sensitivities may have different values. Consult the corresponding article for sensitivity values

and resonators. The mode shift of the waveguide due to light-matter interaction introduces a corresponding phase change which results in a detectable interference fringe shift at the output. Several integrated interferometer mechanisms, such as Mach-Zehnder (MZI), Young (YI), coupler interferometers (CI) are often used as transducing device for sensing. They are highly efficient to make a very small measurement that is not possible by any other means. In resonator sensors, the resonating wavelength shift measures the refractive index changes that arise due to bio-chemical bindings. Thus, high index contrast dielectrics, noble metal and composite material based slot and waveguide sensors could be considered as a one step towards future. Table 14.1 gives an overview of the recently published works on the photonic sensors based on dielectric and hybrid plasmonic slot waveguides with different sensing architectures.

In this chapter, we are presenting dielectric, noble metal and composite material based slot and nanowire for biochemical liquid, gas and vapor sensing. For these results, we used the two and three-dimensional finite element mode solvers and the least-squares boundary residual (LSBR) method for junction analyses. These computational methods are discussed in detail in Chap. 6.

14.3 Detection of DNA Hybridization by Vertical and Horizontal Slot Waveguide

The light confinement in the void nanostructure was first reported by Almeida et al. in 2004 [38], since then the slot waveguide became an intriguing area of research in integrated photonics waveguiding and especially for sensing. A slot waveguide design comprises of the formation of a low index slot region by bringing two narrow high index waveguides close together that are operating below their modal cut-off regions. The lightwave propagates through the low index slot region in between two high index cores. This low index guiding could be justified with the help of electromagnetic boundary condition derivable from Maxwell's equations. It demands that for a high index contrast dielectric interface, the normal component of electric flux density (**D**) must be continuous, i.e. $D_{n1} = D_{n2}$. This, on the other hand, results in a discontinuity of the corresponding electric field (E_n). Thus, a much higher electric field amplitude could be observed in the low index region which enhances and strongly confines the light power into the slot. Utilizing this phenomenon, a much effective light-analyte interaction could be obtained in case of both surface and bulk sensing. The *surface sensing* or *contact sensing* is mostly exploited to measure the refractive index changes of ultra-thin layered film on the waveguides and/or into slot region. An ultra-thin adlayer of receptor molecules uses on guiding material to immobilize the targeted analyte. The binding interaction between the target analyte and adlayer changes the complete (adlayer + analyte) sensing layer thickness that influences the effective index of the guided optical mode. The *bulk sensing* or *homogeneous sensing* refers to another way of sensitivity investigation where the refractive index change of cover and slot regions are detected. Detection of DNA sequencing by hybridization with the help of slot waveguide is investigated by surface sensing where both the SOI-based vertically and horizontally slot geometries were used.

14.3.1 Vertical Slot Waveguide

The novel vertical slot waveguide was designed by keeping two nanometers dimensioned Si cores close together that simultaneously forms a small nano-gap for light guiding. The schematic cross-section of the vertical slot waveguide is shown in Fig. 14.1. The refractive indices of silicon core, silica (SiO_2) substrate were considered as 3.4757 and 1.444, respectively. Cladding and the slot region is filled with deionized (DI) water-based stock solution having $RI = 1.31$. To immobilize the DNA strings, first, the waveguide is coated with a 1 nm ultra-thin receptor linker (silanes or ply-L-lysine) bio-layer (T_L). The detection process consists of sensing of complimentary DNA sequence, where a single stranded DNA (ssDNA) is subsequently combined with a double-stranded DNA (dsDNA). The thickness (T_D) of DNA probe layer was 8 nm, and it remains same after combining with complementary DNA strand. Only detectable change happens in probe layer refractive index, increased from 1.456 (ssDNA) to 1.53 (dsDNA).

The complete waveguide modeling and its performance analyses are carried out by using the **H**-field based FV-FEM. The one-fold symmetry of the waveguide structure is considered, in which more than 80,000 irregular triangular elements have been employed for domain discretization. The structure supports both fundamental quasi-TE and quasi-TM modes. Among all the field components, the E_x

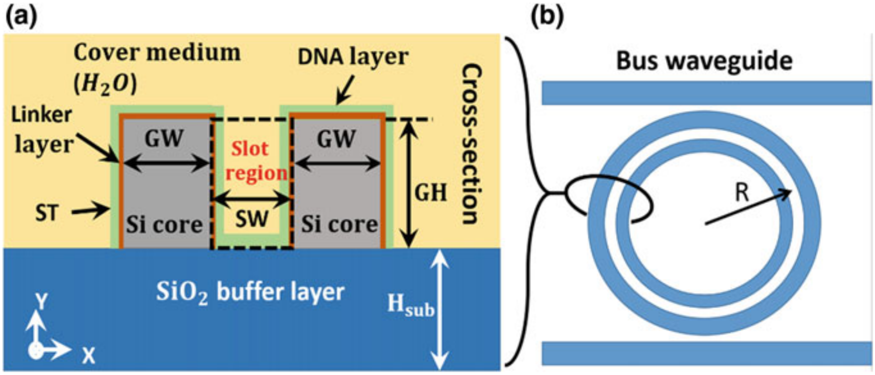

Fig. 14.1 **a** Depicts the schematic cross-section of silicon-on-insulator (SOI) based vertical slot waveguide for detection of DNA hybridization. The slot region is denoted by black dashed line where an enhanced light-matter interaction occurs. **b** Denotes a top-view of a ring resonator incorporated with SOI based vertically slot waveguide

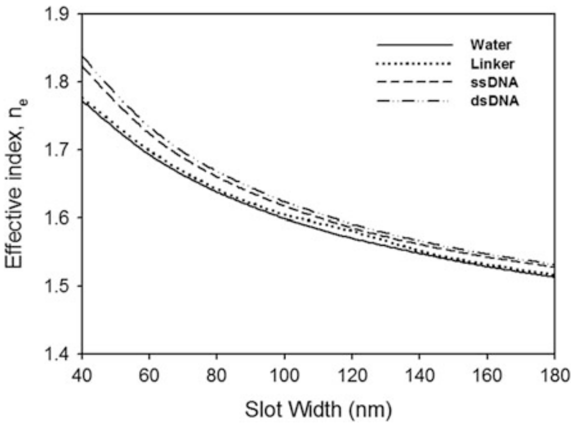

Fig. 14.2 Modal effective index (n_{eff}) variations with slot width (*SW*) for fixed Si core width, $GW = 180$ nm and height, $GH = 320$ nm. From [39]

field of fundamental H_y^{11} mode shows an enhanced discontinuity as the vertical slot is along y-direction. So, in vertical slot only quasi-TE mode shows enhanced confinement in slot region. Figure 14.2 depicts the effective index (n_{eff}) variations of the H_y^{11} mode with the slot width (*SW*) for different waveguiding conditions. Effective index is defined as the normalized propagation constant, $n_{eff} = \beta_0/k_0$ where β_0, k_0 and λ are the modal propagation constant, free-space wavenumber ($k_0 = 2\pi/\lambda$) and operating wavelength, respectively. Si core height (*GH*) and width (*GW*) are considered as 320 nm and 180 nm, respectively. The solid and dotted lines depict the n_{eff} variations for only DI water as cover medium and 1 nm linker layer and water as sensing medium, respectively. The dashed and dashed-dotted lines denote the same for 8 nm ssDNA and dsDNA with water as cover medium. Small slot width confines more power into the slot which enhance the light-analyte interactions. The n_{eff} increase with slot width in Fig. 14.2 also justify this fact. This in-turn also suggest that the change of effective index (Δn_{eff}) due to DNA hybridization waveguide sensitivity also increases with decrease of slot width. Optimizations of the waveguide design parameters are highly effective in order to improve the sensor design for high sensitivity. Measurement of waveguide sensitivity strongly depends on the optical power confinement in the targeted DNA probe layers. Power confinement in the DNA layers have been evaluated and plotted with the variation of the guide width keeping the slot width fixed at 60, 100 and 140 nm and guide height fixed at 320 nm, shown in Fig. 14.3. Although, the lower slot width (60 nm) shows maximum power confinement than followed by 100 and 140 nm slot width however, the 100 nm slot width, is considered for further device optimization and this will also be easy to fabricate compared to other smaller slot dimensions. Thus, a 100 nm slot width (*SW*) with 180 nm guide width (*W*) could be an ideal optimized parameters. It is also noticeable that the ssDNA confines more optical power compared with the dsDNA due to high index contrast of guiding. The waveguide sensitivity can be written as $S_{wg} = \Delta n_{eff}/RI$. Here RI is refractive index of DNA layers and Δn_{eff} is the effective index difference that

Fig. 14.3 Power confinement variations in the DNA layers with the Si core guide width (*GW*) for fixed slot widths, $SW = 60$, 100 and 140 nm. Si core height is fixed at $GH = 320$ nm for all the cases. From [39]

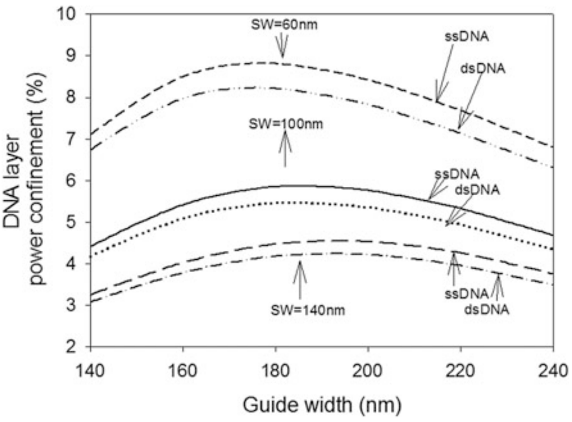

appears due to DNA hybridization. During modelling of DNA hybridization, the effective index difference is obtained by first simulating the ssDNA on top of bio-linker layer and then by considering the combination of the ssDNA with its complementary natured desired ssDNA which forms a layer of dsDNA. Now for the same waveguide structure ($GH = 320$ nm, $SW = 60$, 100 and 140 nm, and GW = variable) the waveguide sensitivity is determined. A greater change in Δn_{eff} makes the bio-sensor more sensitive. Figure 14.4 indicates that a greater Δn_{eff} and waveguide sensitivity for the *GW* in between 200 and 220 nm for all three slot widths. Both the Δn_{eff} and S_{wg} increase with the Si core height (*GH*) and for higher *GH*, most of the power would be started to confine in the Si cores. Thus, the waveguide sensitivity measurement parameters will show an almost saturated variation with high *GH* (not shown here). Therefore, for a compact slot waveguide sensor 320 and 340 nm guide heights are taken here as the desirable dimensions.

To calculate the Δn_{eff} accurately, a compact sensing device containing a slotted ring resonator with 5 μm bending radius is presented and analyzed. The schematic cross-sectional and top views of the device are presented in Fig. 14.1a, b, respectively. The device sensitivity only depends on its component waveguide sensitivity

Fig. 14.4 Effective index difference (Δn_{eff}) and waveguide sensitivity (S_{wg}) variations with the guide width (*GW*). The solid, dashed, and dotted lines indicate three different slot widths, $SW = 60$, 100, and 140 nm, respectively. Si core height was fixed at GH = 320 nm. From [39]

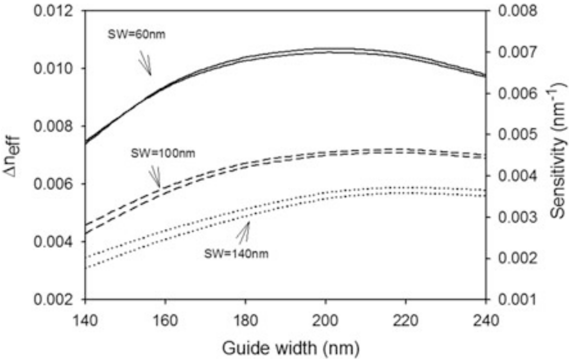

regardless of the type of the devices. Transducing optical parameters are the only way to measure the device sensitivity. Thus, the relation between device sensitivity (S) and resonant wavelength shift ($\Delta\lambda$) can be expressed as

$$S = \frac{\Delta\lambda}{\Delta n} \tag{14.3.1}$$

$$\Delta\lambda = \frac{\Delta n_{eff} \Delta\lambda_{res}}{n_g} \tag{14.3.2}$$

Here Δn_{eff}, λ_{res} and n_g are the effective index change caused by the analyte bindings, resonating wavelength of the ring and waveguide group index, respectively. From Fig. 14.5a, the group index (n_g) is calculated as 1.81264 at the operating wavelength of 1550 nm for the optimized design parameters GW = 220 nm, GH = 320 nm and SW = 100 nm. For performance analysis, the waveguide was simulated once with ssDNA and then with dsDNA to obtain the $\Delta n_{eff} = n_{e,\,ssDNA} - n_{e,\,dsDNA}$. By using Eq. 14.3.2, the wavelength shift of the device is calculated and its variation with Si core width for three different slot widths (60, 100, and 140 nm) are shown in Fig. 14.5b. The slot waveguide with dimensions $GW = 220$ nm, $GH = 320$ nm and $SW = 100$ nm shows that the n_{eff} for ssDNA and dsDNA as a sensing layer were 1.80549 and 1.81264, respectively. A much higher resonance wavelength shift $\Delta\lambda$ = 6.12 nm is achieved and this was calculated by using Eq. 14.3.2. Similarly, by using Eq. 14.3.1, the sensitivity of ring resonator is obtained as 856 nm/RIU.

Due to scattering, the propagation loss of a similar slot waveguide was reported as 12 dB/cm [40]. The absorption spectrum of water shows the absorption value as

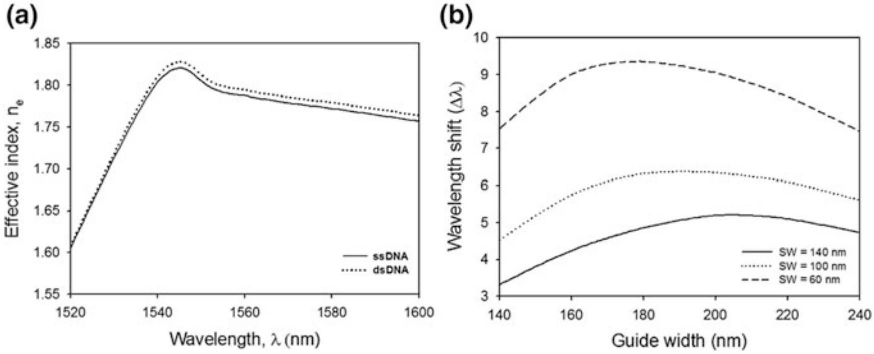

Fig. 14.5 **a** Shows the effective index (n_{eff}) variation of the slot waveguide against operating wavelength. The solid and dotted lines denote the n_{eff} variations due to ssDNA and dsDNA as a sensing layer, respectively; **b** shows the variation of resonating wavelength shift ($\Delta\lambda$) against the Si core guide width during DNA hybridization. The dashed, dotted, and solid lines indicate the variations for SW = 60, 100, and 140 nm, respectively. The Si core height is kept fixed at 320 nm. From [39]

47.5 dB/cm at the wavelength of 1550 nm. Our simulation shows around 30% power confinement in the cover medium that contains DI water. Thus, roughly the total propagation loss of our designed waveguide could be estimated as long as (12 dB/cm + 0.30 × 47.5 dB/cm) = 26.25 dB/cm. So, the total loss for few micron sensor would be very small.

14.3.2 Horizontal Slot Waveguide

Besides vertically slotted waveguide discussed earlier in the previous section, the light enhancement in void nanostructure is also true for a horizontal slot waveguide. A nano dimensioned low index channel along the horizontal x-axis is formed by keeping close two high index dielectric slabs. This geometry is easy to fabricate and often has smoother and regular interfaces exhibiting a much lower modal propagation loss. The fundamental mode supported by this waveguide shows a high discontinuity of E_y field (normal to the material interfaces) in the low index slot region. This would make higher power confinement in the slot region for a quasi-TM H_x^{11} mode. An effective horizontally slotted SOI-based sensor design that uses an enhanced optical power in the low index region, is proposed. Its design parameters optimization and performance analyses for detection of DNA hybridization (surface sensing) are investigated by the FV-FEM.

Such a horizontal slot can be fabricated on SOI substrate, where a low index slot channel is sandwiched by two high index polysilicon slabs. For applications towards bio-chemical or gas sensing, the slot region should be filled by the desired target analytes. Thus, the designed horizontal slot waveguide is connected with the tapered waveguides at both ends to maintain a nanogap by providing support to the suspended top poly-Si layer, as shown in Fig. 14.6a. Initially, a layer-by-layer fabrication on top of SiO_2 substrate is followed to fabricate a multi-layered nanowire, starting from poly-Si then followed by SiO_2 and poly-Si again. Next, a wet

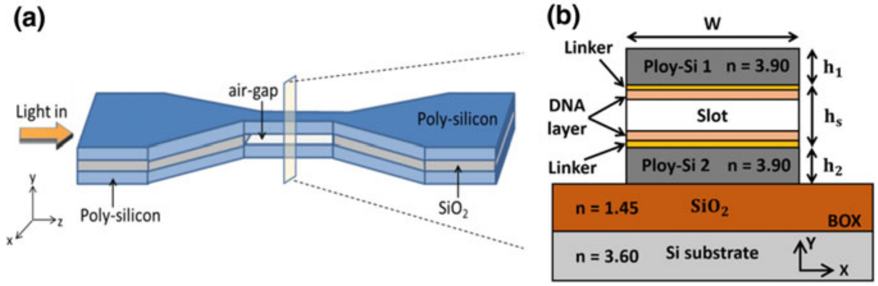

Fig. 14.6 Schematic diagram of the designed SOI based horizontally slotted waveguide for detection of DNA hybridization; **a** shows the 3D structure of the waveguide and **b** depicts a cross-sectional view of the waveguide geometry which is used for computational analysis by FV-FEM. From [41]

etching process using HCL can be followed to remove the middle oxide layer in the less wide slot region. Once the oxide under narrow waveguide region is removed when the etching process is stopped so that the ploy-Si layers can get mechanical support from the tapered section at both ends where the SiO_2 is only partially etched. For optimization and complete analyses of the waveguide as a bio-sensor, a cross-sectional geometry is considered as shown in Fig. 14.6b. The refractive indices and bio-layers thickness of linker layer, ssDNA and dsDNA are taken as same that are used for the previous application. The refractive indices of poly-Si layers, SiO_2 and cover DI water medium are taken as 3.9, 1.444 and 1.33 at the operating wavelength of 1550 nm. In this present work, the key optimization parameters are core width (w), top and bottom poly-Si core heights (h_1 and h_2) and slot height (h_s). For numerical computation, the one-fold symmetry of the geometry is exploited and used more than 34,000 triangular elements for half structured domain discretization. The field components of the fundamental quasi-TM mode are evaluated by mode solver. The E_y field shows the discontinuity at the high index contrast dielectric interface providing the strong field in the slot area. The propagating energy flux density termed as Poynting vector (S_z) is calculated from the **E** and **H** vector fields, is also presented in Fig. 14.7. The 1D line plot of S_z field also shown as an inset. It clearly shows that the optical power is mostly guided by the low index region of slot waveguide.

The power confinement and power density variations in the top and bottom DNA probe layers (8 nm for DNA layer and 1 nm for linker layer) with high indexed poly-Si core height are presented in Fig. 14.8. The power density is the average power confinement per unit area for both DNA probe layers, are shown by the solid lines and power confinement are shown by the dashed lines. Both the power confinement and power density exhibit similar trend with the core height. For smaller core height both the parameters show small values because initially it is closed to the cut-off. Thus, the smaller power confinement occurs due to most of the modal evanescent fields are spread over the substrate and the cladding regions. Modal power increases with the increase of core height, due to enlargement of the guided area, reaches the maximum confinement at a core height, $H = 0.15$ μm. With

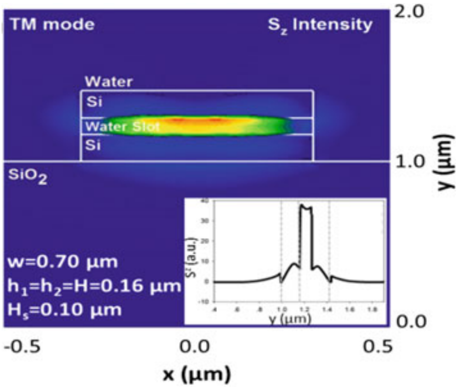

Fig. 14.7 The energy flux density (S_z) of the fundamental quasi-TM mode of the slot waveguide for width (w) = 0.7 μm, poly-Si core height, $h_1 = h_2 = 0.16$ μm and slot height (h_s) = 0.10 μm. From [41]

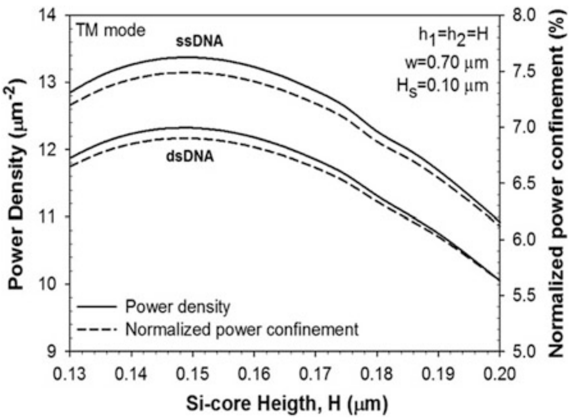

Fig. 14.8 Shows optical power density and power confinement variations in the top and bottom DNA probe layers with poly-Si core height ($h_1 = h_2 = H$) for fixed width, $w = 0.70$ μm and slot height, $h_s = 0.10$ nm. An 8 nm thick DNA probe layer and a 1 nm bio-linker layer ($n_a = 1.42$) are considered for simulations. From [41]

further increment of H, the power confinement decreases due to most of the light guided by the high index Si cores. The effective index change (Δn_{eff}) is one of the important parameter for the analyses of the bio-sensing waveguides, used to determine the sensitivity of the waveguide. The Δn_{eff} variation during DNA hybridization with core height (H) is shown in the Fig. 14.9. The solid and dashed lines denote the waveguide effective index variation (n_{eff}) and Δn_{eff}, respectively. The Δn_{eff} increases with core height until it reaches to the maximum value at height, $H = 0.17$ μm. Beyond this value, the optical power mostly guided by the core rather than the slot. This results reduction of the Δn_{eff} as well as the waveguide sensitivity. Individually, for both the DNA layers the waveguide n_{eff} increases with H because of stronger coupling. Poly-Si core height, $H = 0.15$ μm shows the maximum power confinement into DNA probe layer and $H = 0.17$ μm shows maximum the Δn_{eff} in Figs. 14.8 and 14.9, respectively. Therefore, the optimized poly-Si core height is taken as, $H = 0.16$ μm.

Similarly, the power confinement and power density variation in the sensing layer with the waveguide core width (w) are presented in Fig. 14.10 for a fixed height $H = 0.16$ μm. At smaller width, the power confinement in the sensing layer, shown by the dashed lines, were less due to smaller waveguide size. However, with the core width increment the power confinement slightly increased. Due to high refractive index contrast, the ssDNA shows higher confinement than the dsDNA. Besides, the power density variation shows an inversely proportional trend with w. At smaller width, the small guiding area results in higher power density. As the width increases, the power confinement per unit area reduces due to the larger guiding area. The results indicate that the change in the poly-Si core height (H) is much effective than the core width (w). Next, the dependencies of n_{eff} and Δn_{eff} due to DNA hybridization with the core width (w) are examined and presented in Fig. 14.11. It shows that the n_{eff} values due to both DNA layers, shown by two solid lines, increase with the increasing w. That indicates more light confinement and guidance by the larger waveguide geometry. On the other hand, the Δn_{eff},

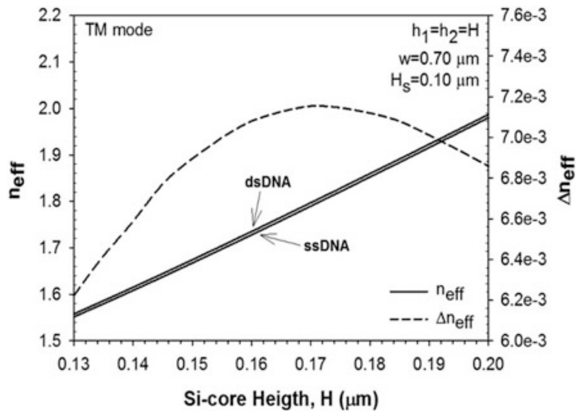

Fig. 14.9 Shows the variations of the effective index (n_{eff}) due to each sensing medium (ssDNA and dsDNA) and the effective index difference (Δn_{eff}) detected during DNA hybridization with Si core height (H). The DNA probe layer comprises of a 1 nm bio-linker layer ($n_a = 1.42$) and an 8 nm ssDNA ($n_b = 1.456$) or dsDNA ($n_b = 1.53$) layer. The core width (w) and slot height (h_s) are fixed at 0.7 and 0.1 µm, respectively. From [41]

Fig. 14.10 Variation of the power density and power confinement in the DNA probe layer with the waveguide core width (w). The other parameters, such as waveguide core height and slot height are fixed at 0.16 µm and 0.10 µm, respectively. From [41]

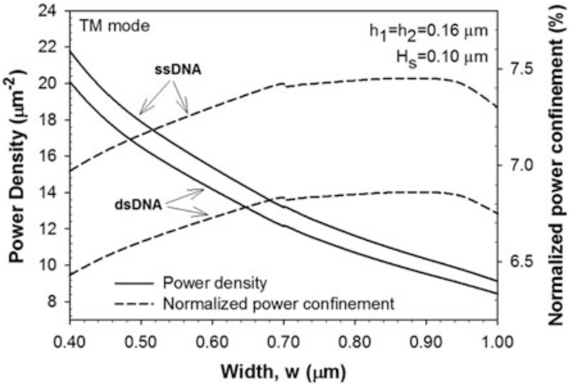

Fig. 14.11 The effective index (n_{eff}) due to individual ssDNA and dsDNA as sensing layer and change in effective index (Δn_{eff}) due to DNA hybridization variations with the core width (w) when the core height and slot height are fixed at 0.16 and 0.10 µm, respectively. From [41]

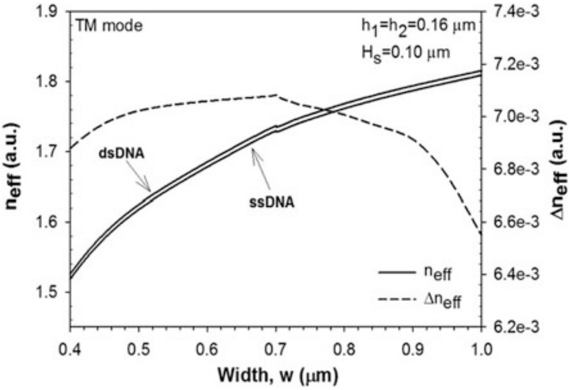

shown by the dashed line, initially increases with increment of w and reaches the maximum value at $w = 0.70$ µm. For $w > 0.70$ µm, the Δn_{eff} shows a decremental trend. Thus, the waveguide design parameters are optimized for the better performance and those can be listed as, $w = 0.70$ µm, $H = 0.16$ µm and $h_s = 0.10$ µm. Although a narrower slot provides a larger Δn_{eff}, but it would be difficult to fabricate a very small and uniform slot due to fabrication limitations. Thus, a 0.10 µm slot height is considered as an optimized value for this design. By looking at the results, it is also noted that the Δn_{eff} is more affected by the poly-Si core height (H) rather than the poly-Si core width (w) as the graph changes more rapidly with the core height.

To detect the Δn_{eff} due to DNA hybridization, this optimized horizontal slot waveguide is incorporated in the sensing arm of an integrated Mach-Zehnder interferometer (MZI) arrangement. The relative phase shift ($\Delta\phi$) depending on the effective index change can be obtained as

$$\Delta\phi = \frac{2\pi}{\lambda} \cdot L \cdot \Delta n_{eff} \tag{14.3.3}$$

where L is MZI arm length incorporated with slot waveguides. The destructive interference with minimum interference signal occurs when the relative phase difference is equal to π. Therefore, even a smaller effective index difference due to DNA sequencing can be measured with this efficient horizontal slot waveguide incorporated MZI transducing device of length 110 µm.

14.4 Cross-Slotted Bio-chemical Sensor

It was shown in Sects. 14.3.1 and 14.3.2 that vertical and horizontal slot guides can only be effective for the quasi-TE and quasi-TM modes, respectively. This signifies that both the designs are strongly polarization dependent. Thus, to overcome this difficulty a novel cross-slot waveguide for biochemical sensing which supports the much stronger field enhancement in the slot region for both quasi-TE and TM mode is designed and rigorously studied. The cross-slot structure is composed of both vertical and horizontal slot regions simultaneously, as shown in Fig. 14.12a.

This structure can be designed to connect via the tapered waveguides and can be fabricated on an SOI wafer with a 220 nm top-Si layer (or a thicker layer if necessary) on a 2 µm or similar thick buried oxide (BOX) layer. If necessary, the top waveguiding silicon layer can be thinned down to an optimized thickness. On top of this, SiO_2 can be deposited through plasma enhanced chemical vapor deposition (PECVD). Following that a low-loss hydrogenated amorphous silicon (a-Si) layer can be deposited followed by a thin SiO_2 layer deposition, which can act as a hard mask, by using PECVD [43]. If necessary these layers can be planarized by using chemical mechanical polishing (CMP), before the next layer deposition. A vertical slot waveguide can be defined by Deep UV (DUV) or

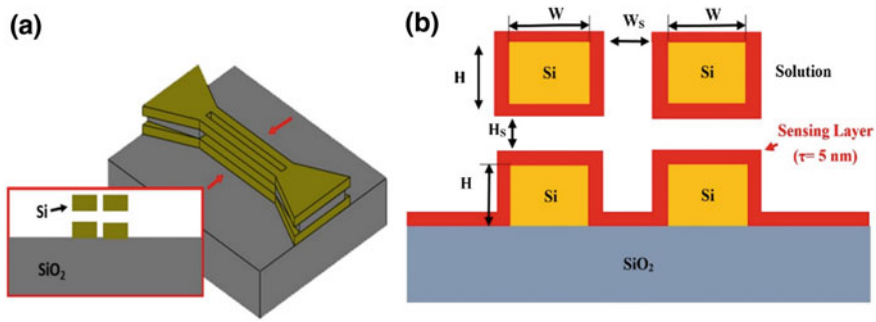

Fig. 14.12 **a** Schematic three-dimensional diagram of the SOI based cross-slot waveguide with hollow vertical and horizontal slots. **b** Cross-sectional view of the cross-slot waveguide used for bio-chemical sensing. A 5 nm bio-sensing layer of refractive index 1.45 is considered for waveguide surface sensing. From [42]

E-beam lithography and followed by dry etching of silicon and SiO_2 layer down to the BOX layer. Next, buffered hydrofluoric acid can be used to etch the SiO_2 layer in between the two horizontal silicon guiding layers to form the horizontal slot [44, 45]. Since the width of the two horizontal slots in between two silicon layers is smaller, hydrofluoric acid introduced through the vertical slot and outside will remove this SiO_2 layer earlier than the much wider SiO_2 layer beyond the vertical slot channel. Once the low-index oxide layer under the narrow waveguide region is removed the etching process is stopped so that two upper silicon layers are mechanically supported by the wider region at the two ends where silica was only partially removed. However, it should be noted that any CMOS compatible material, such as Si_3N_4 [46], can also be used to fabricate the initial slot regions, which later needs to be selectively removed to open the empty slot region. Previously, sensing arm of several microns long incorporating cantilever suspension from one end has been fabricated with negligible deformation [47]. However, since for the proposed structure only a short length of slot waveguide is suspended from both the ends, it is expected to be mechanically sturdier. After the cross-slot WG is formed, the several nm-thick sensing layers for biochemical sensing can be added to all the surface of the silicon cores [17, 25, 45, 48] such as silanized with 3-glycidyloxy propylitrimethoxy saline for label-free protein sensing [17], or dipped into aqueous glutaraldehyde for the study of label-free molecular binding reactions, as shown in Fig. 14.12b. Here the thickness of sensing layer is taken as 5 nm.

The 2D-FEM simulated E_x and E_y field profiles for the quasi-TE and TM modes are shown in Fig. 14.13a, b, respectively. For the quasi-TE mode, the power confinement factor in the total slot region (Γ_{T-Hy}) increases, reaches its peak value and then decreases with the increase of silicon core width (W). This peak value also increases with the increase of silicon core height (H). Similarly, the total-slot confinement factor (Γ_{T-Hx}) for quasi-TM mode shows a similar variation tendencies but with H and W. Thus, $\Gamma_{T-Hy} + \Gamma_{T-Hx}$ is taken as an optimization parameter

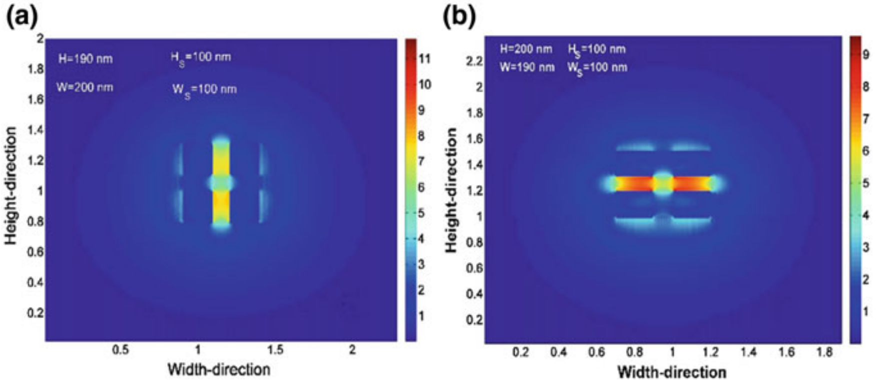

Fig. 14.13 Low index guided **E** field profile of the fundamental modes with different polarizations in the cross-slot waveguide. **a** E_x—field profile of the H_y^{11} mode, E_y-field profile of the H_x^{11} mode. All the field profiles are generated by using 2D-FEM. From [42]

to maximize the total-slot confinement. This parameter shows total 79% power confinement for silicon core width and height 205 nm and 220 nm, respectively. Besides, the ratio of the total-slot confinement factors for the H_y^{11} and H_x^{11} modes ($\Gamma_{T-Hy}/\Gamma_{T-Hx}$) is another important parameter for optimization to make the device polarization independent. Variations of $\Gamma_{T-Hy}/\Gamma_{T-Hx}$ with the width, W and height, H of silicon cores are shown in Fig. 14.14a, b, respectively. The ideal ratio of 1 is shown here by a black dashed line. It can be observed from Fig. 14.14a that for a given height, due to the parabolic variation tendency of Γ_{T-Hy} and the monotone-increasing variation tendency of Γ_{T-Hx} with the silicon core width, all the ratios increase initially and then decrease with the increase of the silicone core width. The red curve for $H = 250$ nm shows that the cross-slot WG can confine equal power in the whole slot region for both the polarizations, but total-slot confinement factor for each one is around 34%. On the other hand, for $H = 220$ nm, shown by a green line, total-slot confinement factor for each polarization can reach to the same value of 39.3%, when the silicon core width is taken as 212 nm. Again, for a given width, the confinement ratios decrease at first and then increase with the increase of the silicon core height, as shown in Fig. 14.14b. It is obvious that the ratio can reach 1 at several width and height combinations. To achieve a successful polarization-independent design, the sensitivities for the H_y^{11} and H_x^{11} modes should be not only nearly the same but also large enough, so the width and height of the silicon cores are optimized to be around 223 and 216 nm, with the total-slot confinement factor for each polarization of 39.4%. It can also be observed here that the performance would be remarkably stable even for a possible ±10 nm fabrication error of the silicon core dimensions.

Figure 14.15 gives the cross-slot dimension optimization based on surface sensitivity, $S = \Delta n_{eff}/\Delta\tau$. A bio-layer with completely saturated with analyte of

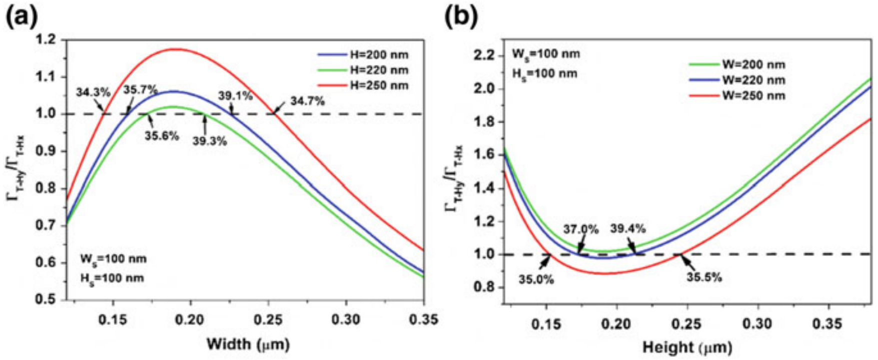

Fig. 14.14 Variations of the ratio $\Gamma_T - H_y/\Gamma_T - H_x$ with **a** the Si core width, W and **b** height, H. From [42]

Fig. 14.15 Cross-slot waveguide sensitivities with the horizontal and vertical slot dimensions for different polarizations. The solid and dashed lines show the sensitivity variations with the horizontal slot height (H_s) and vertical slot width (W_s), respectively. From [42]

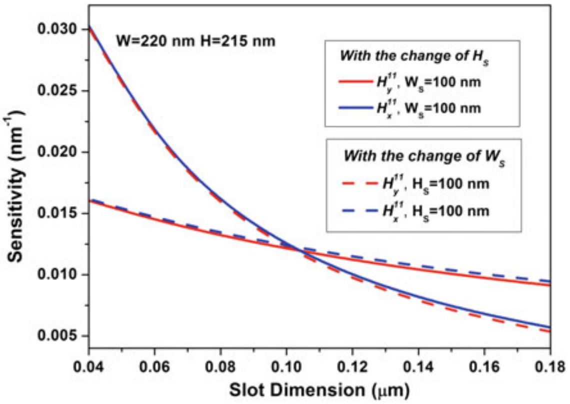

thickness $\Delta\tau = 5$ nm and refractive index of 1.45 is considered. It can be observed that with the decrease of the width or the height of cross-slot, the sensitivities for both the two polarization modes increase. However, the sensitivity for H_y^{11} mode increases more quickly when the cross-slot width decreases, while that for H_x^{11} mode increases more quickly with the decrease of slot height. When both the cross-slot width and height are set to 100 nm, the sensitivity value for each polarization mode is 0.012 nm^{-1}, which is twice the same of vertical-slot-waveguide or horizontal-slot-waveguide sensors with similar dimensions. Obviously, the sensitivities for both H_y^{11} and H_x^{11} modes can be improved synchronously by reducing the width and height of cross-slot simultaneously.

14.5 Straight Vertical Slotted Resonator

Slot waveguide is very attractive in sensing applications because of its enhanced light-matter interaction inside the low index slot region. So far, many refractometric sensing devices have been reported where a slot waveguide is incorporated in the ring resonators. However, a ring resonator also suffers from bending loss and coupling losses with the bus waveguides. Instead of a ring resonator with comparative larger device footprint, a nanometer-scaled straight vertically slotted resonator has been designed. The three-dimensional resonating device is shown in the Fig. 14.16. The main device of interest contains two high index straight silicon cores separated by a narrow slot channel. This resonating structure is coupled with the in and out bus waveguides. The tunable light from the laser travels through the bus waveguide and excites the slotted structure at a particular wavelength. During the resonance condition, the electromagnetic energy builds up in the slot cavity and allows to pass that particular light wavelength from input bus to output bus waveguide. Thus, the resonance wavelength (λ_{res}) can be detected by the photodetectors (not shown) at both facets of output bus waveguide (λ_{out1} and λ_{out2}) and at the opposite end of the input bus waveguide. The complete resonating structure is designed and its sensing ability is investigated at the widely-used telecommunication wavelength, λ = 1550 nm. The silicon slot guide is separated by a silicon dioxide (SiO_2) buffer layer from the silicon substrate. The silicon and silicon dioxide refractive indices are taken as $n_{\mathrm{Si}} = 3.476$ and $n_{\mathrm{SiO_2}} = 1.44$, respectively at the 1550 nm operating wavelength. The key advantages of this device can be explained in three steps. First, the nanometer dimension results high scale integration and ease of fabrication than other complex devices. Second, the dominant E_x field of the quasi-TE mode shows high magnitude inside the slot that results a in strong light-matter interaction. Third, a much-improved device sensitivity (S) and detection limit (DL) can be achieved with help of first two steps. For sensing applications, the slot and surrounding medium can be filled with any low index solution of one's interest.

The CMOS compatible fabrication process of this curve free device is simple compared to other photonic sensing devices. The two rails of Si core can easily be fabricated by the etching of unwanted Si into a commercially available SOI wafer. Besides, if required further increment of the Si core height can be achieved by precise control of Si layer growth with the help of plasma enhanced chemical vapor deposition (PECVD). A photoresist thin film is deposited on the Si layer for slot patterning. Then the reactive ion-etching (RIE) process can be followed to make Si core strips with a slot region in between them.

The 3D slotted resonator is shown in Fig. 14.16 is a short length straight vertical slot waveguide. Therefore, the rigorous investigation of the design parameters, calculation of dominant and non-dominant field components, profiles of for the fundamental quasi-TE and TM modes and power confinement into the different guiding region are done with the help of 2D FV-FEM. Throughout the 2D-FEM simulations, 1,280,000 first order triangular elements are used for computational domain discretization. After completion of the device design, the 3D FV-FEM is used to determine the modal solutions and performance analyses of the 3D slotted resonator. Two different sensing mechanisms, both bulk and surface sensing have been considered here. A 5 nm ultra-thin sensing layer (T_s) is taken for bio-molecular detection, as shown in the bottom inset of the Fig. 14.16. The high sensitivity of the device strongly depends on the power confinement (Γ) in the region where the light and targeted analyte interaction occurs. Thus, optimization of the slot's cross-sectional design parameters, such as Si core width (W), height (H) and low index slot width (W_s) are much important. Both the total slot confinement ($\Gamma_{slot-total}$) and confinement into 5 nm sensing layer ($\Gamma_{slot\ sensing\ layer}$) increases with W, reach their maximum values and then decrease [49] for a fixed Si core height (H) and slot width (W_s). The maximum confinement into slot and sensing layer and corresponding W indicates the optimized value of Si core width (W). Now with a fixed W and W_s, the Si core height (H) variation shows that the $\Gamma_{slot-total}$ and $\Gamma_{slot\,sensing\,layer}$ continuously increase with H. However, the power density initially increases, reaches a maximum and then decrease with H [49]. Although, the variation of the effective index shift (Δn_{eff}) due to presence of 5 nm sensing layer shows an excellent correlation with the $\Gamma_{slot-total}$ variation. Although, in practice, a 220 nm Si height is widely used as it is the typical thickness of most commonly available Si in SOI wafer, however, in this case, the higher core height yields better sensors, so the optimized Si core height (H) is taken as 500 nm that can also be easily fabricable with modern technology [50]. Finally, a further investigation on slot width (W_s) shows a maximum confinement, $\Gamma_{slot-total} = 43.8\%$ could be achieved by the optimized slot waveguide design parameters as, Si core width (W) = 170 nm, Si core or slot height (H) = 500 nm and slot width (W_s) = 130 nm. The cover medium and the slot region are considered to be filled with aqueous solution of refractive index 1.33. By using 2D FV-FEM again, the effective index (n_{eff}) of the optimized slot structure is evaluated and it was 1.63827.

The vertical slotted cavity supports the longitudinal modes at the specific resonating wavelength (λ_{res}) and that can be defined as

$$\lambda_{res} = \frac{2L \cdot n_{eff}}{m} \tag{14.5.1}$$

Here $2L$ is the round-trip length of the longitudinal electromagnetic wave in the resonator and m = 1, 2, 3… denotes the order of supported longitudinal modes. Equation 14.5.1 indicates that the number of longitudinal modes strongly depends on the resonator length (L). As the fundamental mode is expected to be more stable and sensitive than the higher order modes, the slot resonator cavity length (L) has been calculated for a single (m = 1) longitudinal fundamental mode using Eq. 14.5.1. Finally, all the device design parameters can be summarized as, Si core width (W) = 170 nm, core or slot height (H) = 500 nm, slot width (W_s) = 130 nm and the device length (L) = 473 nm for a specific resonating wavelength, λ_{res} = 1550 nm.

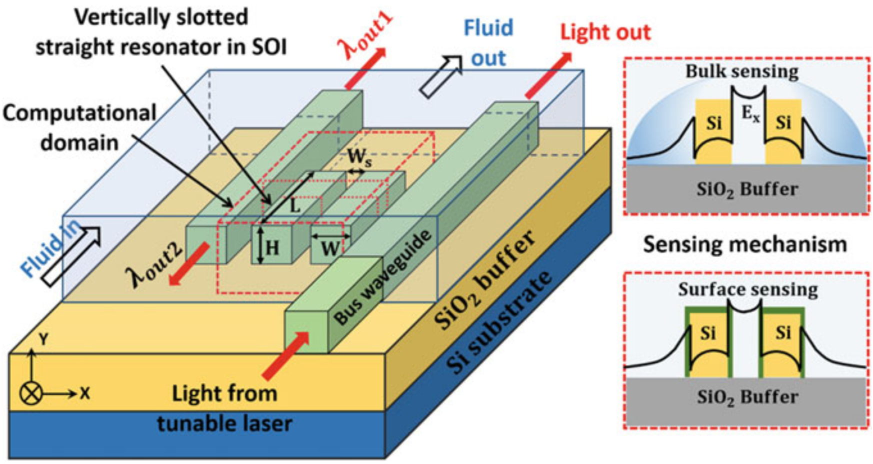

Fig. 14.16 Schematic diagram of the three dimensional (3D) vertically slotted straight resonator. The right sided insets bordered with red dashed lines show the sensing mechanisms considered for the refractometric sensing analyses. From [49]

In a resonating cavity, the self-consistent longitudinal field gets confined and oscillates at a particular wavelength. Thus, the further performance investigations require a complete three-dimensional analysis of the quasi-TE and TM modes inside the resonating structure. A dedicated rigorous and full vectorial **H**-field based three-dimensional finite element method (3D-FEM) is developed and used to solve the problem. All the field components of the resonating modes can be generated by the post-processing of the eigenvectors obtained from complete device simulation by the 3D FV-FEM. The 3D iso-surface profile of the dominant and most sensitive E_x field of the slotted resonator is simulated by the 3D-FEM shown in Fig. 14.17. During 3D-FEM simulations over 456817 first order tetrahedral elements are considered for the three-dimensional computational domain discretization of dimensions 1.47 μm (along x) × 0.473 μm (along y) × 1.5 μm (along z). Its performance analyses divided into two stages: (1) *surface sensing,* where an ultra-thin bio-molecular layer covers the sensing device surface (Fig. 14.16, **bottom inset**) and (2) *bulk sensing*, where refractometric changes of the homogeneous medium are considered (Fig. 14.16, **top inset**).

14.5.1 Surface Sensing

In case of surface sensing, a thick bio-layer (linker + bio-molecular layer) of refractive index 1.45 have considered on top of both Si strips and the slot region. The cover medium is filled with the aqueous solution (n_{water} = 1.33). The 3D-FEM computation measured a 5.2 nm resonating wavelength shift for a 5 nm sensing

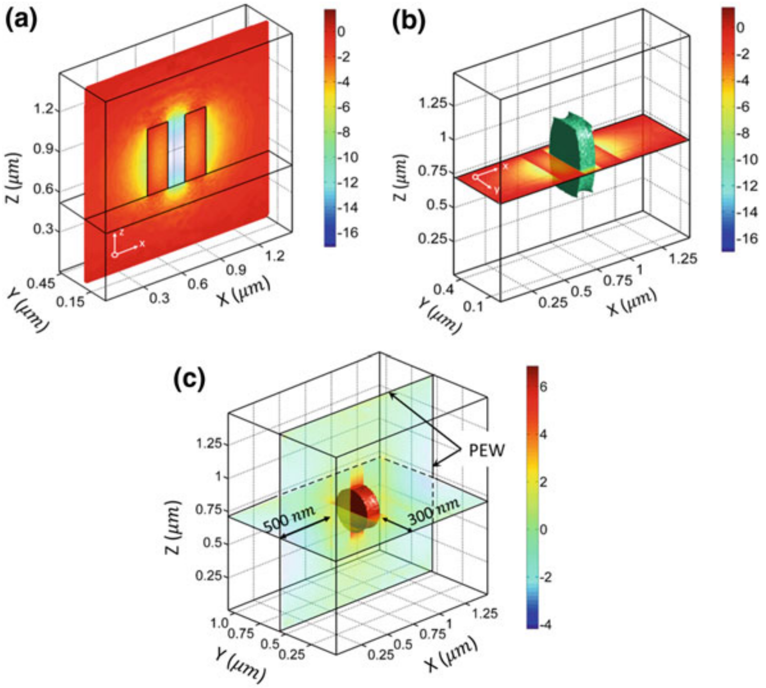

Fig. 14.17 2D and 3D profiles of the dominant E_x field confined into a straight single slotted resonator at the resonating wavelength, $\lambda_{res} = 1550$ nm; **a** shows the E_x field profile at the mid-sliced x-z plane of the slot resonator, **b** depicts the 3D iso-surface profile of the E_x field where boundary walls are considered to be placed at both end faces of the Si cores, **c** shows the 3D E_x field when the boundary walls are placed away from the both end faces and side faces of the Si strips. A 3D FV-FEM is used for complete resonating structure simulations. From [49]

layer of refractive index, $n = 1.45$. The device sensitivity has been investigated for different thickness of sensing layers ranging from 5 to 50 nm. The surface sensitivity of the device can be defined as

$$S_{surface} = \frac{\Delta\lambda_{res}}{\Delta t} \tag{14.5.2}$$

Here, $\Delta\lambda_{res}$ and Δt are the resonance wavelength shift and corresponding bio-layer thickness change. The $\Delta\lambda_{res}$ linearly increases with the thickness of sensing bio-layer shown by the red solid line in Fig. 14.18. Thus, $\Delta\lambda_{res}$ and bio-layer thickness change (Δt) shows a strong linear relationship. Similarly, the variation of the surface sensitivity of the device against different bio-layer thickness is shown by the green diamond markers, plotted using a high-resolution scale. Thus, the Fig. 14.18 shows a small reduction of $S_{surface}$ with an increase of bio-layer thickness.

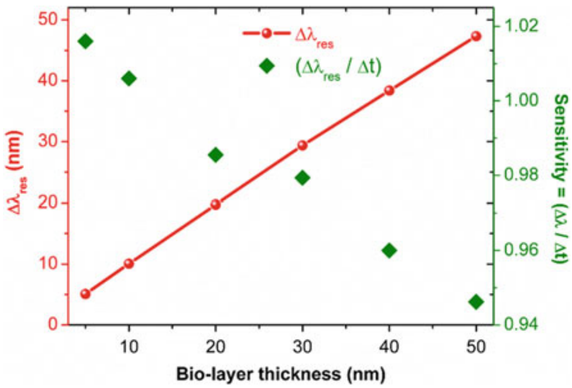

Fig. 14.18 Surface sensing of the designed device with optimized design parameters. The redline shows a linear response of wavelength shift ($\Delta\lambda_{res}$) for different bio-layer thickness of refractive index 1.45. The green diamond markers denote the surface sensitivity ($S_{surface}$) variation with bio-layer thickness ranging from 5 to 50 nm. From [49]

14.5.2 Bulk Sensing

The bulk sensing process follows the detection of the refractive index change of the homogeneous bulk medium in the cover and slot regions. For rigorous investigations, aqueous sucrose solutions with different concentrations are used over the sensing device. The refractive indices of sucrose solution for different sucrose concentration at ambient temperature (20 °C) are taken from the datasheet [51]. Similar to practical situations, two different cases have been investigated in the simulation process: (1) the cover and slot region are completely filled with the sensing fluid, and (2) only cover medium is filled with the fluid and the slot is filled with air bubbles.

The bulk refractometric sensitivity of the vertically slotted waveguide has been investigated by 2D-FEM. The low index guided E_x-field profile and its response to the homogeneous refractive index change are shown in Fig. 14.19. The variation of the normalized effective index change ($\Delta n_{eff}/n_{eff}$) with refractive index changes of the sucrose solution presents a linear relationship, shown by a red line. The bulk sensitivity of the waveguide structure can be determined from the slope of the curve as $S_{bulk} = \left(\Delta n_{eff}/n_{eff}\right)/RIU$ and its value was calculated as 1.025 per RIU. In case of the 3D resonating device, the bulk sensitivity can be defined as

$$S_{bulk} = \frac{\Delta\lambda_{res}}{RIU} \tag{14.5.3}$$

Here $\Delta\lambda_{res}$ and RIU denote the resonating wavelength shift of the device and the refractometric change due to different concentration of sucrose in the solution, respectively. The resonating wavelength change ($\Delta\lambda_{res}$) of the designed structure as a function of the sucrose solution refractive index are shown in Fig. 14.20. The solid and dashed lines show the device responses when the boundary electric walls are placed both ends of and far away from the Si strips, respectively. A strong linear shift is observed by the lines and its slope i.e. sensitivity (S_{bulk}) show the value of

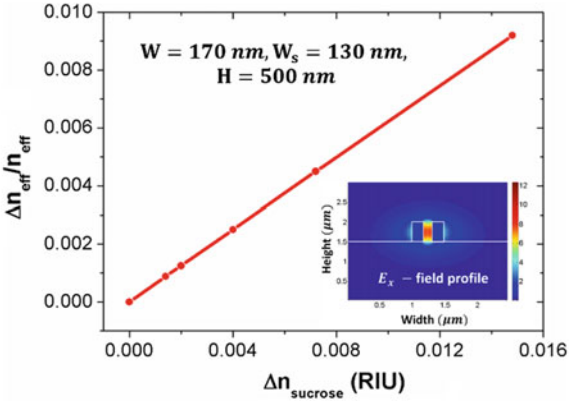

Fig. 14.19 Bulk refractometric sensitivity analysis of the vertically slotted waveguide with optimized design parameters, such as, $W = 170$ nm, $W_s = 130$ nm and $H = 500$ nm at 1550 nm operating wavelength. The curve slope denotes the sensitivity of the waveguide when the cover medium is fully covered with the sucrose solution. The inset shows the 2D-FEM simulated E_x-field profile that is essential for low index guiding sensing. From [49]

635 nm/RIU and 335 nm/RIU for the fully filled and empty slot cases. The empty slot condition may arise when the sensing liquid may not enter slot region due to the presence of air bubbles. A better response of the resonator device could be obtained when the boundary walls are placed away from the Si strip end faces. Fluid-Si contact at both ends increases in this case that also increases the device sensitivity, shown by the blue and green dashed lines in Fig. 14.20. The slope of the linear resonance wavelength shift indicates a much high device sensitivity of 820 nm/RIU and 683 nm/RIU for filled and empty slot cases, respectively. Besides the spectral shift the detection limit (*DL*) of the device can be estimated from the device sensitivity (S_{bulk}) and the sensor resolution (R) as, $DL = \mathrm{R}/S_{bulk}$. The device resolution strongly

Fig. 14.20 Resonating wavelength shift of the proposed device versus refractive index variation ($\Delta n_{sucrose}$) of sucrose solution at ambient temperature (20 °C). The solid and dashed lines denote the device bulk sensitivity when the electric walls are kept at the end faces and away from the end faces from Si strips. The slope of each linear curve presents bulk sensitivity (S_{bulk}) for the filled and empty slot conditions. From [49]

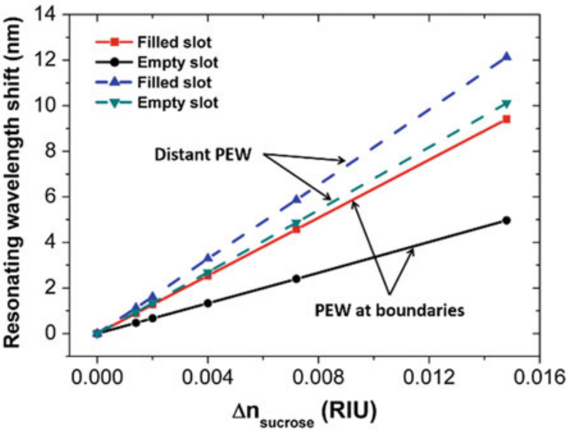

depends on the wavelength resolution ($\lambda_{resolution}$) of the laser source. A laser source with wavelength resolution of 5 pm indicates that a minimal detectable refractive index of 7.9×10^{-6} RIU and 6.1×10^{-6} RIU could be achieved for the boundary walls touching the end facets and away from the Si strips, respectively.

A rigorous least-squares boundary residual (LSBR) [52] method is used to determine different coupling parameters of the coupled Si bus waveguides and the slotted resonating structure for different gaps. The junction interface between input guide and the resonator slot section shows some back reflections of the input signals. Those reflection coefficients (ρ_r) have been calculated as 0.024, 0.020, and 0.012 for three different separations 250, 300, and 450 nm, respectively. On the other hand, the coupling losses at the junction interface are calculated as 0.2886, 0.1956, and 0.0833 dB for all three mentioned separations. It shows that the 250 nm gap provides higher evanescent coupling the slot resonating structure but with higher coupling loss, whereas the 400 nm gap provides less evanescent coupling with higher coupling efficiency. Therefore, 250–400 nm could be considered as suitable separation range for this coupling between bus waveguide and slot resonating structure.

14.6 Plasmonic Gas Sensing by Al^{+3} Doped ZnO Coated Au Nanowire

Metal oxides have been extensively used in sensing devices. Among them, zinc oxide (ZnO) has attracted considerable interests for different areas, such as sensing [53], lasing [54], light harvesting [55] and detection [56]. Similarly, gold (Au) nanoparticles have also received much attention due to its plasmonic properties at visible wavelengths. In this section, an Au nanocore with an Al^{+3} doped ZnO (AZO) cladding layer has been designed and studied by using the **H**-field based full-vectorial finite element method (FV-FEM) for use as an optical gas sensor. In the numerical simulations, the wavelength dependent Au and ZnO refractive indices are taken from [57, 58], respectively. A small concentration of Al^{+3} doping in ZnO results in an effective replacement of Zn atoms by Al atoms which increase the conductivity of doped ZnO. This in turn also modify the plasmonic frequency of the AZO thin film that can be described by the Lorentz-Drude model [59] as follows

$$\varepsilon_\omega = \varepsilon_{ZnO} - \frac{\omega_p^2}{\omega_p^2 + j\gamma\omega} \tag{14.6.1}$$

Here ε_{ZnO} is the optical dielectric constant of ZnO and ω_p is the plasma frequency, defined by $\omega_p = Ne^2/\varepsilon_0 m^*$ with N as the carrier concentration in the range of 1×10^{17} to 1×10^{20} cm^{-3}. The γ denote the carrier damping constant given by $\gamma = e/\mu m^*$. Here the electron mobility μ has been considered as 24 cm^2/Vs for the

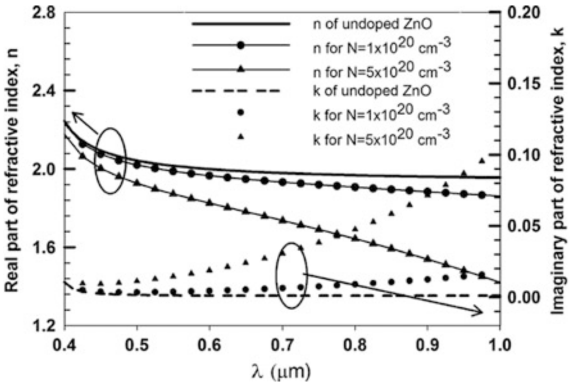

Fig. 14.21 Real and imaginary refractive index variations with the wavelength for ZnO and AZO. The Lorentz-Drude model is used for refractive index calculation. From [61]

target Al^+ of 2 w.% (weight ratio). m^* denotes the effective mass that has been taken as the 0.24 times of the electron mass. Figure 14.21 presents the real and imaginary parts of ZnO and AZO with the carrier concentration of $N = 1 \times 10^{20}$ cm^{-3} and 5×10^{20} cm^{-3}. The refractive index of ZnO is nearly 2.0 for visible wavelengths and tend to rise while reaching the UV direct band edge of ZnO at 3.3 eV. The figure illustrates that an increase in the carrier concentration reduces the AZO refractive index and this reduction is greater for longer wavelengths. Due to increased conductivity of AZO, the imaginary part of the refractive index also increases. Thus, the loss is higher for longer wavelengths and also for higher doping levels.

As a practical device, a finite dimension AZO coated Au nanowire with height, $h = 60$ nm and width, $w = 250$ nm is considered, as shown in the inset of Fig. 14.22. A 100 nm of AZO cladding around the metal core, which is also surrounded by the infinite air cladding is considered for computation analysis. In the simulation, it has been observed that the modal propagation length (L_p) of the waveguide is around 3 μm for an AZO cladding with lower carrier concentration, $N_L = 1 \times 10^{17}$ cm^{-3}. With the increase of carrier concentration, the refractive index of AZO reduces from its undoped ZnO value and as a result, the effective index of the quasi-TM mode decreases. Additionally, as N increases the material loss also increases due to increasing conductivity. Therefore, the change in effective index and differential loss could be the important parameters for sensing investigations.

$$\Delta n_{eff} = \left| n_{eff}(N_L) - n_{eff}(N) \right| \tag{14.6.2}$$

$$\Delta Loss = |Loss(N_L) - Loss(N)| \text{ in dB/mm} \tag{14.6.3}$$

Here N_L and N are the fixed (1×10^{17} cm^{-3}) and variable doping carrier concentration. The curves in Fig. 14.22 depict the variations of Δn_{eff} and $\Delta Loss$ with the carrier concentration, N. It can be seen that Δn_{eff} changes linearly with the carrier concentration. On the other hand, $\Delta Loss$ increases with N but tends to saturate at a high carrier concentration. This is due to the fact that as the N

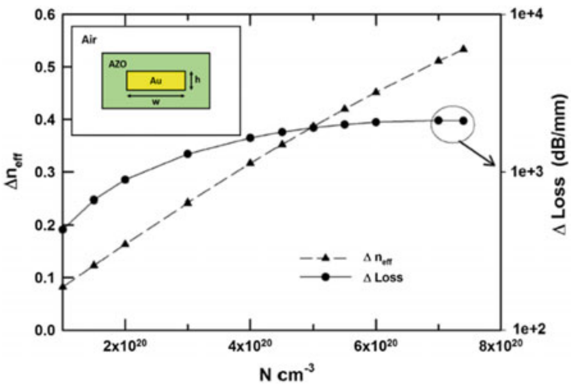

Fig. 14.22 Δn_{eff} and $\Delta Loss$ variations with the carrier concentration of AZO cladding at the operating wavelength, λ = 750 nm. The inset is showing the schematic cross-section of the plasmonic waveguide where a finite Au core is cladded with AZO layer. The dimension of the Au core is taken as, width (w) = 250 nm and height (h) = 60 nm. From [61]

increases, the refractive index of AZO decreases and simultaneously the modal power confinement in the AZO cladding reduces from a value of ~80% at $N_L = 1\times 10^{17}$ cm^{-3} to a value ~55% at $N = 7.4\times 10^{20}$ cm^{-3}. In the case of finite cladded Au nanowire, reducing the width of the core tends to reduce $\Delta Loss$ and Δn_{eff} as a large amount of power leaks into the surrounded air cladding. Thus, the width changes of the Au core and its effect has not been analysed rather a fixed core width, w = 250 nm has been considered for further investigations.

Electrons are the majority charge carrier in the AZO. Therefore, absorption of gas and vapor liquid on the AZO surface will deplete electrons, resulting in a decrease in conductivity. The Debye length is used to quantify the thickness of the space charge layer that has deficient carriers due to electron trapping by the chemisorbed oxidizing agent in the n-type semiconductor. The Debye length of the AZO layer is taken as 10 nm [60] for the carrier concentration of the order of 10^{17} cm^{-3}. Initially, the Au core dimension of w = 250 nm and h = 60 nm with $N = 7.4\times 10^{20}$ cm^{-3} has been considered. It has also been assumed that the N in the depletion region is changing from $N_{D,L} = 7.4\times 10^{20}$ cm^{-3} to a value of $N_{D,L} = 10^{17}$ cm^{-3} for a Debye depth equivalent to 10 nm. For simplicity, a uniform depletion of the carrier concentration also has been taken at the AZO boundaries. A large cladding thickness makes the core far away from the depletion layer. Thus, the quasi-TM mode do not get affected by the higher degree by the refractometric change in the depletion layer. When the cladding thickness is very small, a large portion of the modal power might spread into the outer air cladding region. Therefore, cladding thickness is considered as an important parameter for optimization. Figure 14.23 depicts the effective index change (Δn_{eff}) as a function of AZO thickness for three different operating wavelengths, such as 650, 700 and 750 nm. Above 90 nm thickness, the effective index change is larger for λ = 750 nm, compared to that of $\lambda = 650$ nm. When the cladding thickness is larger, around 100 nm, the surface plasmon mode guided by the core has a spot size area that is two to three times larger than that of $\lambda = 650$ nm. This allows a higher proportion of the modal power in the depletion region, as shown by the Γ_D

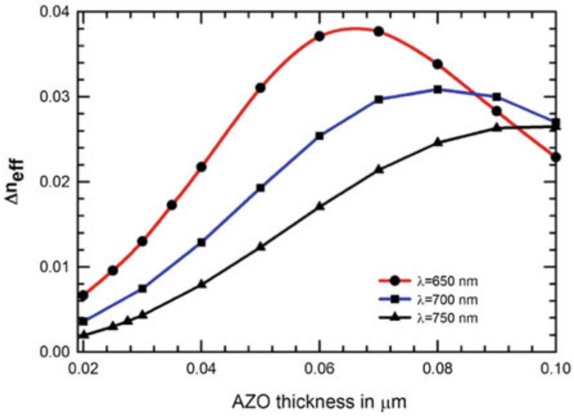

Fig. 14.23 Variation of real effective index change of the waveguide with the cladding thickness at three different operating wavelengths 650, 700, and 750 nm. From [61]

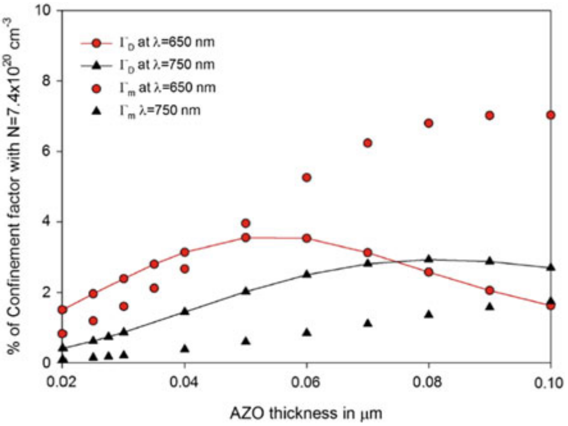

Fig. 14.24 Variation of power confinement (%) in the depletion (Γ_D) and metal core (Γ_m) with respect to the AZO cladding thickness. Two operating wavelengths, λ = 650 and 750 nm. From [61]

variations in the Fig. 14.24. Additionally, at 650 nm the metal core shows higher power confinement compared to that in the depletion region. Furthermore, the Δn_{eff} is larger for longer wavelengths. Due to these factors, for large AZO thickness ~100 nm, the Δn_{eff} is higher for longer wavelengths. It can be seen in the Fig. 14.23, for the lower thickness (<80 nm) the Δn_{eff} is higher at $\lambda = 650$ nm than that of $\lambda = 750$ nm. As the depletion region is closer to the metal core, the confinement in the depletion region (Γ_D) becomes larger for those operating wavelengths.

Figure 14.25 presents the percentage change of the modal propagation length, $L_p = 1/2\beta_i$ (β_i is the imaginary part of the propagation constant) with respect to the AZO cladding thickness. The percentage change of the modal propagation length ($\Delta L_p\%$) can be calculated as

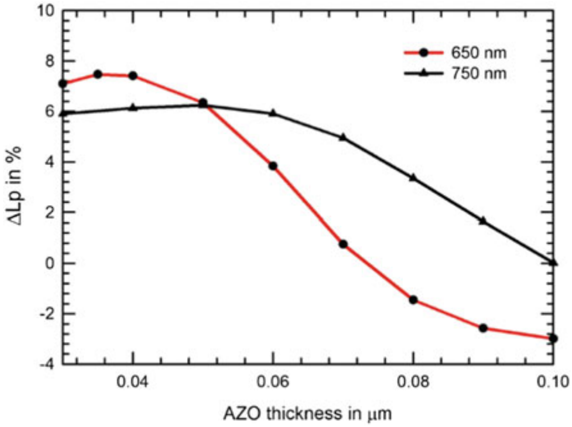

Fig. 14.25 Variations of the change in the propagation length (ΔL_p) as a function of AZO cladding layer thickness at two different wavelengths, λ = 650 nm and 750 nm shown by the red and black lines, respectively. From [61]

$$\Delta L_p\% = \left(1 - \frac{L_p(N_{D,L})}{L_P(N_{D,H})}\right) \times 100 \qquad (14.6.4)$$

The red ($\lambda = 650$ nm) and black ($\lambda = 750)$ nm) lines in Fig. 14.25 indicate that as the cladding thickness decreases, the modal propagation length change (ΔL_P) rises from its negative and reaches a maximum value. Further reduction of thickness starts leakage of a higher proportion of power in the air cladding and thus, the ΔL_p starts to decrease. For a larger thickness, the ΔL_p shows negative value whereas, for lower AZO thickness ΔL_p becomes positive. For a lower thickness of AZO cladding the confinement in both the depletion (Γ_D) and metal core (Γ_m) decrease. Furthermore, due the close position of the depletion and metal core influences the surface plasmonic mode such that the modal loss increases with the increasing refractive index in the depletion layer. With the help of these rigorous analyses, it has been shown that for finite AZO cladding thickness (20–100 nm), the depletion of carriers for a depth equivalent to Debye length can affect the modal effective index variation that is greater than 0.035 and a variation of the propagation length which is greater than 5%. These waveguide modal properties can be exploited by incorporating this plasmonic waveguide into a Mach-Zehnder based opto-chemical sensor.

14.7 Ethanol Vapor Sensor by Composite Plasmonic Waveguide

Now a day, ethanol (CH_3CH_2OH) is one of the most important constituents in daily life, from chemical and pharmaceutical products to heavy engineering and fuel industries. Mixing of excessive ethanol vapor with air may cause explosive fire with an easy ignition. Only 3.5% ethanol vapor in the air can causes fire explosions, and this often called as *lower explosion limit* (LEL). On the other hand, the upper explosion limit (UEL) of ethanol is 19% [62]. Therefore, for accurate sensing of ethanol vapor in the industrial environment several sensing mechanisms can be considered, such as spectrometric sensing, electrochemical, sloid state semiconductor and microcontroller based devices. However, the dielectric waveguide based interferometric and resonating sensing devices are more convenient for its high precision sensitivity and compactness. Here a horizontal slotted composite plasmonic waveguide (CPWG) is designed and its performance has been rigorously investigated by incorporating it into a Mach-Zehnder interferometer (MZI) device. The novel CPWG is composed of lossy silver (Ag) layer, porous ZnO (P-ZnO), silicon (Si) and silica (SiO_2). The P-ZnO layer is sandwiched in between metal and high index Si, shown in Fig. 14.26a. This novel waveguide structure guides the light through its low index slot region as a supermode that is a coupled form of the surface plasmon (SP) mode and dielectric waveguide mode. Surface plasmon polaritons (SPPs) are the surface waves tightly confined at the metal-dielectric interfaces. The SP mode is TM-polarized in nature and that can be excited either by electrons or photons having same frequency and momentum. Here the CPWG is designed and optimized for the widely used telecommunication wavelength, $\lambda =$ 1550 nm. This waveguide supports both quasi-TE and TM modes. However, the plasmonic supermode which is quasi-TM polarized is concentrated in the low index region, whereas, the quasi-TE mode is guided by the high index Si core. The analytical and semi-analytical solutions to exploit the hybrid plasmonic mode is not so easy. Thus, a full-vectorial **H**-field based modified FEM is used as a computational tool for the device design and performance analyses. For accurate simulations, the one-fold symmetry of the CPWG is discretized with 1,280,000 triangular elements. A much higher mesh density is used near the metal-dielectric interfaces to resolve the sub-wavelength SP field confinements. The optical properties of the silver (Ag), Si and SiO_2 are taken as $n_{\mathrm{Ag}} = 0.13880 + \mathrm{j}\ 11.310$ [63], $n_{\mathrm{Si}} = 3.4757$ [64] and $n_{\mathrm{SiO_2}} = 1.4440$ at the operating wavelength of 1550 nm. The electromagnetic boundary condition at the material interface demands the continuity of the normal component of electric flux density (**D**) at the interface that results in an enhanced E_y-field discontinuity at that interface. The FV-FEM simulated E_y and H_x field components of the fundamental quasi-TM mode are shown in the Fig. 14.26b, c, respectively.

The porous ZnO (P-ZnO) is used as a low index medium which shows a comparative lower index than that of bulk ZnO, as the P-ZnO contains air ($n_{air} = 1$) pores. To make the waveguide efficient for sensing, different types of P-ZnO layer templates can be used, such as porous flakes composed of ZnO spheres, P-ZnO nanosheets, and nanoplates. All these P-ZnO templates are mesoporous where the pore diameters are ranging from 2 to 50 nm. Different templates show its best response and selectivity at different operating temperatures. The P-ZnO sphere layer shows a great selective response to 100 ppm ethanol at 280 °C [65]. Similarly, the strong ethanol selectivity can be observed around 400–450 °C for nanosheets [66] and nanoplates [67], respectively. Thus, in terms of selectivity, all these P-ZnO

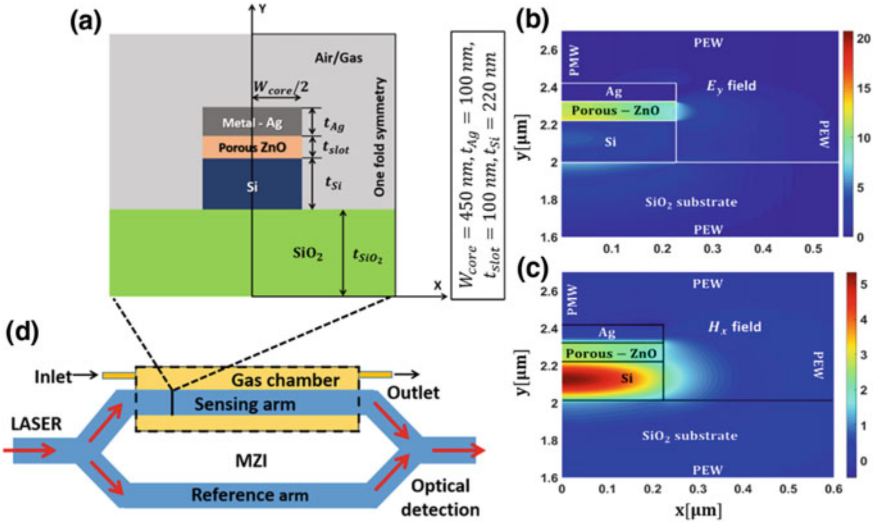

Fig. 14.26 Schematic diagram of a horizontal slotted CPWG and its simulated field distributions, **a** shows the waveguide cross-section. One-fold symmetry of the structure is used for FV-FEM simulations. **b** and **c** are the E_y and H_x field profiles of fundamental quasi-TM mode (H_x^{11}), respectively. **d** Shows a compact, integrated Mach-Zehnder set-up where the CPWG is used in the interferometer arms. From [70]

configurations show excellent ethanol selectivity compared to methanol, acetone, chlorobenzene, and methane at 280, 400 and ~450 °C. When the porous layer is placed in the target analyte vapor, the void pores are then filled with the condensed analyte ($n > 1$). Depending on different volume fraction of absorbed and condensed ethanol, the equivalent index as well as the dielectric constant of P-ZnO changes. To determine the effective refractive index of P-ZnO and the equivalent refractive index of ethanol absorbed P-ZnO, the Lorentz-Lorenz model [68] is used.

$$\frac{n_e^2-1}{n_e^2+2}=(1-P)\left(\frac{n_c^2-1}{n_c^2+2}\right)+(P-V)\left(\frac{n_a^2-1}{n_a^2+2}\right)+V\left(\frac{n_d^2-1}{n_d^2+2}\right) \qquad (14.7.1)$$

Here P denotes the number of pores per unit volume, called *porosity* of the medium and V is the volume fraction of liquid after capillary condensation. n_a, n_c and n_d represent the refractive index of air ($n_a = 1$), homogeneous (bulk ZnO) and dispersed medium (condensed vapor), respectively. For the investigations, the P-ZnO layer of porosity P = 30, 40, 50 and 60% are considered. Corresponding refractive index variations ($n_{P-\mathrm{ZnO}}$) and equivalent refractive index of the P-ZnO with respect to the different volume fraction of ethanol are shown in Fig. 14.27. As expected, the $n_{P-\mathrm{ZnO}}$ decreases with the increasing porosity in the medium shown by the black solid line. Additionally, while the P-ZnO pores are replaced by the condensed ethanol the equivalent index of refraction increases for P-ZnO layers

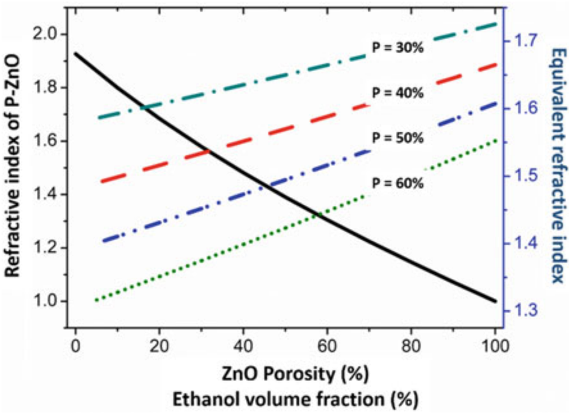

Fig. 14.27 Refractive index variation with ZnO porosity (P) and change of equivalent refractive index of P-ZnO layer with volume fraction (V) of condensed ethanol. From [70]

with P = 30, 40, 50 and 60%. The lower porosity (P = 30%) shows higher equivalent refractive index than the higher porosity (P = 60%). At ambient temperature (20 °C), the bulk ZnO refractive index is taken as 1.9267, derived from the dispersion formula in [69] and the condensed ethanol refractive index is derived by using the Sellmeier equation.

$$n^2(\lambda) - 1 = \frac{A_1\lambda^2}{\lambda^2 - B_1} + \frac{A_2\lambda^2}{\lambda^2 - B_2} \tag{14.7.2}$$

Here $A_{1,2}$ and $B_{1,2}$ denotes the material property parameters and absorption wavelengths. The constant values used for the analysis are, $A_1 = 0.83189$, $A_2 = -0.15582$, $B_1 = 0.00930\ \mu\text{m}^{-2}$ and $B_2 = -49.45200\ \mu\text{m}^{-2}$.

To obtain a high sensitive accurate CPWG, its design parameters, such as core width (W_{core}) and low index slot thickness (t_{slot}) are needed to be optimized carefully. For simplicity, fixed Si nanowire height and top Ag layer thickness have been considered as 220 nm and 100 nm, respectively. Figure 14.28 shows the power confinement variations of the fundamental quasi-TM and TE modes with slot thickness (t_{slot}) for three different CPWG core width, W_{core} = 350, 450, and 550 nm. For all three CPWG core widths the quasi-TM power confinements (Γ_{TMslot}), shown by solid lines, increase with t_{slot} increment, reach a maximum value of 41.79% at $t_{slot} = 70$ nm and then decrease gradually with further increment of t_{slot}. It can also be seen that the $W_{core} = 450$ nm, shown by the red solid line, confines higher optical power than other two core widths (350 and 550 nm). Additionally, the quasi-TE power confinement (Γ_{TEslot}), shown by dashed-dotted lines, increases with the increment of t_{slot}. But these values are much lower than the TM mode confinement. The curves for all three core widths intersect each other at 68 nm and exhibits only 3.56% power confinement. Thus, optimized t_{slot} value is taken as 70 nm with maximum power confinement in the slot region. Furthermore, the optimization of core width (W_{core}) has been carried out for two different t_{slot} = 70 and 100 nm and the results are presented in Fig. 14.29. As the W_{core} increase the

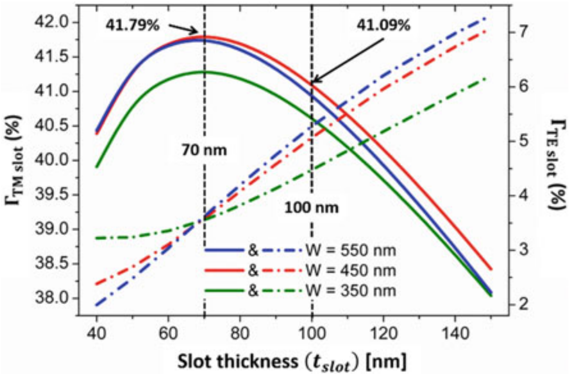

Fig. 14.28 Quasi-TM and TE slot confinement variations with slot thickness (t_{slot}). The TM and TE slot confinement for three different core widths, W_{core} = 350, 450 and 550 nm are denoted by solid and dashed-dotted green, red and blue lines, respectively. From [70]

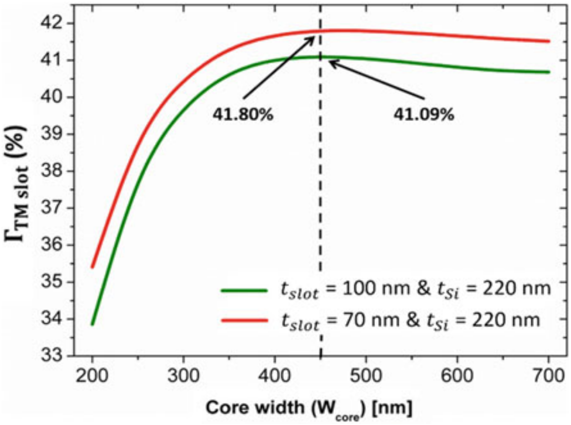

Fig. 14.29 Quasi-TM slot confinement (Γ_{TMslot}) with respect to the CPWG core width (W_{core}) for two different slot thicknesses. The red and green lines denote the same variations for t_{slot} = 70 nm and 100 nm, respectively. An over 41% power confinement is observed for W_{core} = 450 nm at t_{slot} = 70 nm and 100 nm. From [70]

Γ_{TMslot} grows and confines maximum 41.80% and 41.09% TM energy into 70 and 100 nm slots, respectively at $W_{core} = 450$ nm. From both the figures, it can be observed that a 100 nm slot can confine 41.09% power in the low index region. As the $t_{slot} = 70$ nm and 100 nm show a small difference in Γ_{TMslot} and a few nanometers extra wide may be convenient to accommodate more numbers of pores in mesoporous ZnO layer as well as be easier to fabricate. Thus, finally the optimized t_{slot} is considered as 100 nm.

Next, the efficiency of ethanol vapor detection with the help of CPWG is analyzed. The quasi-TM and TE real effective index difference ($\Delta Re(n_{eff})$) of the CPWG with the volume fraction of ethanol for different P-ZnO are shown in Fig. 14.30. The solid lines in the main figure and dashed lines in the inset represent the TM-$\Delta Re(n_{eff})$ and TE-$\Delta Re(n_{eff})$ variations, respectively. Both the effective index difference between TM and TE modes increase with the increment of the volume fraction of ethanol. The higher porosity (60%) shows better effective index difference than that of lower porosity (30%) P-ZnO. Furthermore, the $\Delta Re(n_{eff})$ for TM mode shows much higher values than that for the TE mode. This indicates that

Fig. 14.30 Quasi-TM and TE effective index changes ($\Delta Re(n_{eff})$) against volume fraction of ethanol into P-ZnO layer. The black, red, blue and green solid and dashed lines in main and inset depict the TM and TE modal effective index change due to different volume fraction of ethanol into 30%, 40%, 50% and 60% porous P-ZnO layers, respectively. From [70]

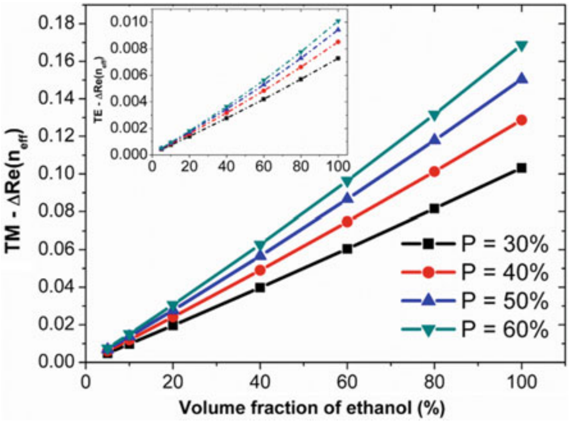

the hybrid plasmonic quasi-TM mode is more sensitive in compare to the quasi-TE mode. Figure 14.31a, b depict the waveguide TM modal sensitivity variations for both real and imaginary effective index. The black, red, blue and cyan markers denote the real effective index sensitivity ($S_{Re(TM)} = \Delta Re(n_{eff})/\Delta n_{slot}$) and normalized attenuation sensitivity ($S_{Im(TM)} = \Delta Im(n_{eff})/\Delta n_{slot}$) of the fundamental quasi-TM mode for porosity, P = 30%, 40%, 50% and 60%, respectively. For each P-ZnO layer the $S_{Re(TM)}$ and $S_{Im(TM)}$ initially decreases up to ~15% of ethanol absorption and then increases with the increase of volume fraction of ethanol. The sensitivity curves also indicate that the P-ZnO layer with lower porosity (P = 30%) shows higher $S_{Re(TM)}$ and $S_{Im(TM)}$ than that of the higher porosity (P = 60%). In case of waveguide based sensor, the $S_{Re(TM)}$ is much important than $S_{Im(TM)}$ and here a much higher $S_{Re(TM)}$ (≈0.71 per RIU) can be obtained with this novel design CPWG. Besides, the Fig. 14.31b depicts that the $S_{Im(TM)}$ is significantly less sensitive to slot refractometric changes.

Effective index change of the CPWG due to analyte's refractometric variation is the only detectable parameter for a waveguide-based sensor. Thus, for accurate measurement of this effective index change, a compact Mach-Zehnder interferometer (MZI) can be used as a transducer device. The MZI schematic diagram is shown in Fig. 14.26d where the designed and optimized CPWG is incorporated in MZI arms. One arm is passed through the ethanol vapor chamber to measure the volume fraction of ethanol, is called *sensing arm* and other is used as a *reference arm*. The phase difference between both arms can be derived from the detectable effective index change $\Delta Re(n_{eff})$ due to a different percentage of absorption of ethanol into P-ZnO.

$$\Delta\phi = \frac{2\pi}{\lambda} \cdot \Delta Re(n_{eff}) \cdot L \tag{14.7.3}$$

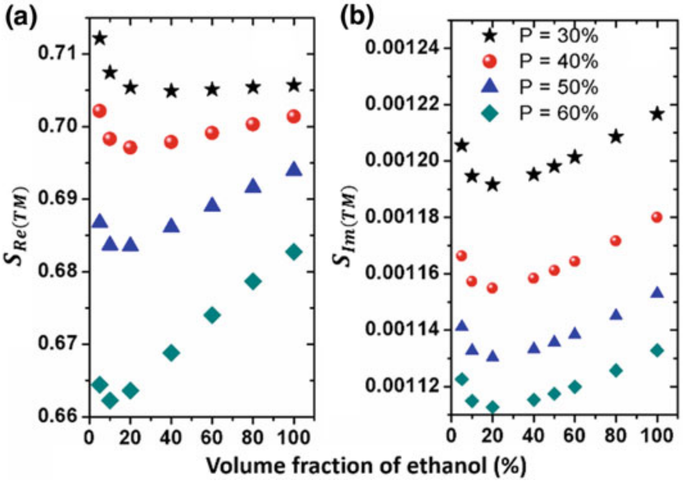

Fig. 14.31 **a** and **b** present the quasi-TM real effective index sensitivity ($S_{Re(TM)}$) and normalized attenuation sensitivity ($S_{Im(TM)}$) variations with volume fraction of ethanol, respectively. The black, red, blue and cyan markers on both figures denote the sensitivity variation with absorbed ethanol into low index P-ZnO slot with porosity, P = 30%, 40%, 50% and 60%, respectively. From [70]

Here L denotes the CPWG arm length. A π phase difference between reference and sensing arm makes a destructive interference with a zero MZI output. By using the fact in Eq. 14.7.3 the MZI arm lengths are calculated as 7.51, 6.02, 5.15 and 4.59 μm for each type of P-ZnO layer having porosity P = 30%, 40%, 50% and 60%, respectively. Thus, higher porosity gives higher Δn_{eff} that results in shorter MZI length (L). All these CPWG incorporated MZI arms show a much low propagation loss around 0.2 dB for each aforementioned arm lengths. It can also be seen that with and without ethanol vapor absorption the waveguide modal loss changes in PWG incorporated MZI arms are 0.045 dB for P = 30%, 40% and 50% and 0.047 dB for P = 60%, respectively. Often it is assumed that the attenuation (α) of the incorporated waveguide is same for both MZI waveguides. However, in case of the CPWG in sensing, both the sensing and reference arms may show different attenuations, $\alpha_{ref} = \alpha$ and $\alpha_{sen} = \alpha \pm \Delta\alpha_{sen}$, respectively. It is considered that the sensing waveguide arm attenuation is modified by a small change $\Delta\alpha_{sen}$ due to different absorption levels of ethanol vapor. Therefore, including this attenuation change, the normalized power output of the MZI can be expressed as [70]

$$P_{norm} = \frac{1}{2} e^{-2\alpha L} e^{-\Delta\alpha_{sen} L} cosh(\Delta\alpha_{sen} L)(1 + Fcos\Delta\phi) \tag{14.7.4}$$

Here, the parameter F is defined as the interferometric fringe contrast and it can be defined as, $F = 1/\cosh(\Delta\alpha_{sen} L)$. Additionally, a part of the Eq. 14.7.4 could be

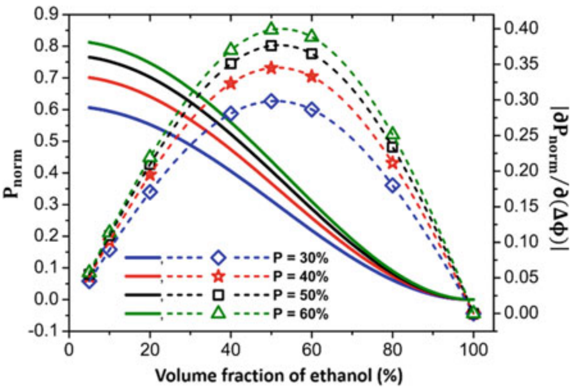

Fig. 14.32 Normalized power output (P_{norm}) and phase sensitivity ($|\partial P_{norm}/\partial(\Delta\phi)|$) variations of the MZI against volume fraction of ethanol absorbed into P-ZnO layer. The blue, red, black and green solid and dashed lines with markers denote the cosine natured P_{norm} and sinusoidal $|\partial P_{norm}/\partial(\Delta\phi)|$ variations for different porosity, $P = 30\%$, 40%, 50%, and 60%, respectively. From [49]

termed as *power fraction*, $PF = e^{-\Delta\alpha_{sen}L} cosh(\Delta\alpha_{sen}L)$. It denotes the sensing arm power increment or decrement compared to reference arm waveguide. The P_{norm} is the only measurable parameter of the MZI that changes with the resulting phase difference. Thus, the MZI phase sensitivity could be defined as

$$\frac{\partial P_{norm}}{\partial(\Delta\phi)} = -\frac{1}{2} e^{-(2\alpha+\Delta\alpha_{sen})L} cosh(\Delta\alpha_{sen}L) F sin(\Delta\phi) \tag{14.7.5}$$

In this CPWG incorporated MZI, the balance between both arms may break due to different attenuations ($\alpha_{ref} \neq \alpha_{sen}$). Hence to make the device error free the attenuation in both arms should be controlled such that it does not interfere with the MZI balance. In this design, for all the volume fractions of ethanol into P-ZnO having porosity, P = 30, 40, 50, and 60%, the fringe contrast is ~0.99 and the power fraction (*PF*) is ~0.96 ($F \approx PF \approx 1$). Thus, the extra attenuation change in the sensing waveguide is very small to cause any noticeable effect in the MZI performance. The Fig. 14.32 depicts the normalized power (P_{norm}) and absolute value of the phase sensitivity ($|\partial P_{norm}/\partial(\Delta\phi)|$) variations with respect to the volume fraction of ethanol for different P-ZnO layers. The results indicate that 100% ethanol vapor absorption in sensing arm makes a π phase difference with zero output and a minimum 5% volume fraction of ethanol provides a minimum phase difference with maximum 60%, 70%, 76%, and 81% light output for 30%, 40%, 50%, and 60% P-ZnO, respectively. The high porosity in P-ZnO provides better light output. Blue, red, black and green markers with dashed lines show a sinusoidal variation of phase sensitivity for all four P-ZnO layers. The higher porosity (P = 60%) shows better phase sensitivity than that of the lower porosity (P = 30%). It can also be seen that for all P-ZnO layers with different porosity, P = 30%, 40%, 50% and 60% exhibit maximum phase sensitivities of 0.30, 0.34, 0.38 and 0.40 when 51.57%, 52.05%, 52.59% and 53.16% of the P-ZnO pores are filled by the condensed ethanol, respectively when an exact $\pi/2$ phase difference is observed in between sensing and the reference arms. Thus, with the help of numerically simulated investigation a label-free ethanol vapor or gas sensor using a coupled SPP and dielectric field confined in a low index horizontal slot is designed and demonstrated.

14.8 Conclusions

In this chapter, a range of compact micro and nano dimensioned integrated optical sensors are designed and optimized its performance for biochemical and gas sensing applications. The results suggest that the on-chip integrated dielectric, plasmonic and composite plasmonic waveguides and resonators have a great potential to be used for high precision sensing and detection technologies. Different numerical methods, such as 2D-FEM, 3D-FEM, and LSBR have been formulated and successfully used to analyse these photonic devices.

Recently published works on slot-waveguide based photonic devices have proved their advantages over conventional waveguides in many ways, such as enhanced and easy-accessible low index light confinement for sensing, trapping, manipulation of nanoparticles, biomolecules and opto-mechanical transducers. These exotic waveguides and resonators could be easily realized by CMOS compatible high index contrast materials and noble metals, such as Si/SiO_2, Si_3N_4/SiO_2, and SOI in combination with Au, and Ag metals. The reported applications in refractive index based liquid and gas detection, labeling-based and label-free biochemical detection, optical trapping, transport and manipulation bio-molecules lead us to a progressive improvement of nano-bio technology. However, standardization and commercialization of these devices require further attention on improved waveguiding design schemes, material engineering, modern sensing architectures, compatibility and assembly of photonic devices with electronic devices, and real-time signal processing.

References

1. E.A.J. Marcatili, Dielectric rectangular waveguide and directional coupler for integrated optics. Bell Syst. Tech. J. **48**, 2071–2102 (1969)
2. J.E.A. Goell, A circular-harmonic computer analysis of rectangular dielectric waveguides. Bell Syst. Tech. J. **48**, 2133–2160 (1969)
3. R.M. Knox, P.P. Toulios, Integrated circuits for the millimeter through the optical frequency range, in *Proceedings of the Symposium on Submillimeter Waves* (Poly Inst., Brooklyn, 1970), pp. 497–516
4. E.K. Sharma, A.K. Ghatak, I.C. Goyal, Matrix method for determining propagation characteristics of optical waveguides. IEEE J. Quantum Electron. **19**, 1231–1233 (1983)
5. N. Dagli, C.G. Fonstad, Analysis of rib dielectric waveguide. IEEE J. Quantum Electron. **21**, 315–321 (1985)
6. K.N. Bierwirth, M. Schulz, F. Arndt, Finite-difference analysis of rectangular dielectric waveguide structures. IEEE Microwave Theory Technol. **MTT-34**, 1104–1114

7. M.S. Stern, P.C. Kendall, P.W.A. Mcllroy, Analysis of the spectral index method for vector modes of rib waveguides. Proc IEEE J. Optoelectron. **137**, 21–26 (1990)
8. U. Rogge, R. Pregla, Method of lines for analysis of strip-loaded optical waveguides. J Opt. Soc. Am. B **8**, 459–463 (1991)
9. B.M.A. Rahman, J.B. Davies, Finite-element solution of integrated optical waveguides. J. Lightwave Technol. **2**, 682–688 (1984)
10. B.M.A. Rahman, J.B. Davies, Penalty function improvement of waveguide solution by finite-element. IEEE Trans. Microwave Theory Technol. **32**, 20–28 (1984)
11. P.P. Silvester, R.L. Ferrari, *Finite Elements for Electrical Engineers* (Cambridge University Press, 1990)
12. A.D. Berk, Variational principles for electromagnetic resonators and waveguides. IRE Trans. Antennas Propag. **4**, 104–111 (1956)
13. K.T.V. Grattan, T. Sun, Fiber optic sensor technology: an overview. Sens. Actuator A-Phys. **82**, 41–61 (2000)
14. L.S. Grattan, B.T. Meggitt (eds.), *Optical Fiber Sensor Technology: Fundamentals* (Springer, US, 2001)
15. Y. Saito, Y. Kanaya, A. Nomura, T. Kano, Experimental trial of a hollow-core waveguides used as an absorption cell for concentration measurement of NH_3 gas with a CO_2 laser. Opt. Lett. **18**, 2150–2152 (1993)
16. C.A. Barrios et al., Slot-waveguide biochemical sensor. Opt. Lett. **32**, 3080–3082 (2007)
17. C.A. Barrios et al., Label-free optical biosensing with slot-waveguides. Opt. Lett. **33**, 708–710 (2008)
18. V.M.N. Passaro et al., Efficient chemical sensing by coupled solt SOI waveguides. Sensors **9**, 1012–1032 (2009)
19. R.J. McCosker, G.E. Town, Optical chemical sensor using a multi-channel directional coupler with slot waveguides, in *International Conference on Photonics* (ICP) (2010), pp. 1–5
20. F. Dell`Olio, V.M.N. Passaro, Optical sensing by optimized silicon slot waveguides. Opt. Express **15**, 4977–4993 (2007)
21. L. Vivien et al., Vertical multiple-slot waveguide ring resonators in silicon nitride. Opt. Express **16**, 17237–17242 (2008)
22. X. Tu et al., Thermal independent Silicon-nitride slot waveguide biosensor with high sensitivity. Opt. Express **20**, 2640–2648 (2012)
23. A. Kargar, C.Y. Chao, Desigh and optimization of waveguide sensitivity in slot microring sensors. J. Opt. Am. A **28**, 596–602 (2011)
24. I. Khodadad et al., Optimization of multiple-slot waveguides for biochemical sensing. App. Opt. **53**, 5169–5178 (2014)
25. T. Claes et al., Label-free biosensing with a slot-waveguide-based ring resonator in silicon on insulator. IEEE Photonics J. **1**, 197–204 (2009)
26. J.I. Kou, F. Xu, Y. Lu, Loop-mirror-based slot waveguide refractive index sensor. AIP Adv. **2**, 042142-1–042142-6 (2012)
27. Q. Liu et al., Highly sensitive Mach-Zehnder interferometer biosensor based on silicon on nitride slot waveguide. Sens. Actuator B-Chem. **188**, 681–688 (2013)
28. Q. Liu et al., A refractive index sensor design based on grating-assisted coupling between a strip waveguide and a slot waveguide. Opt. Express **21**, 5897–5909 (2012)
29. G.D. Osowiecki et al., Vertically coupled plasmonic slot waveguide cavity for localized biosensing applications. Opt. Express **22**, 20871–20880 (2014)
30. X. Sun et al., High-sensitivity liquid refractive-index sensor based on a Mach-Zehnder interferometer with a double-slot hybrid plasmonic waveguide. Opt. Express **23**, 25688–25699 (2015)
31. X. Sun et al., Double-slot hybrid plasmonic ring resonator used for optical sensors and modulators. Photonics **2**, 1116–1130 (2015)
32. W. Zhou, Fully suspended slot waveguides for high refractive index sensitivity. Opt. Lett. **42**, 1245–1248 (2017)

33. L. Zhou, Miniature microring resonator sensor based on a hybrid plasmonic waveguide. Sensors **11**, 6856–6867 (2011)
34. X. Wang, C.K. Madsen, Highly sensitive compact refractive index sensor based on phase-shifted sidewall Bragg gratings in slot waveguide. App. Opt. **53**, 96–103 (2014)
35. J.T. Robinson, L. Chen, M. Lipson, On-chip gas detection in silicon optical microcavities. Opt. Express **16**, 4296–4301 (2008)
36. B. Kumari et al., Silicon-on-nitride slot waveguide: a promising platform as mid-IR trace gas sensor. Sens. Actuator B-Chem. **236**, 759–764 (2016)
37. B. Kumari, R.K. Varshney, B.P. Pal, Design of chip scale silicon rib slot waveguide for sub-ppm detection of N_2O gas at mid-IR band. Sens. Actuator B-Chem. **255**, 3409–3416 (2018)
38. V.R. Almeida et al., Guiding and confining light in void nanostructure. Opt. Lett. **29**, 1209–1211 (2004)
39. T. Dar, J. Homla, B.M.A. Rahman, M. Rajarajan, Label-free slot-waveguide biosensor for the detection of DNA hybridization. Appl. Opt. **51**, 8195–8202 (2012)
40. C. Koos et al., All-optical high-speed signal processing with silicon-organic hybrid slot waveguides. Nat. Photonics **3**, 216–219 (2009)
41. C. Viphavakit, M. Komodromos, C. Themistos et al., Optimization of a horizontal slot waveguide biosensor to detect DNA hybridization. Appl. Opt. **54**, 4881–4888 (2015)
42. C. Pan, B.M.A. Rahman, High-sensitivity polarization-independent biochemical sensor based on silicon-on-insulator cross-slot waveguide. IEEE J. Sel. Top. Quantum Electron. **23**, 64–71 (2017)
43. R. Sun et al., Horizontal single and multiple slot waveguides: optical transmission at λ = 1550 nm. Opt. Express **15**, 17967–17972 (2007)
44. S. Lee et al., A silicon nitride microdisk resonator with a 40-nm-thin horizontal air slot. Opt. Express **18**, 11209–11215 (2010)
45. S. Lee et al., Label-free optical biosensing using a horizontal air-slot SiN_x microdisk resonator. Opt. Express **18**, 20638–20644 (2010)
46. J. Chee, S. Zhu, G.Q. Lo, CMOS compatible polarization splitter using hybrid plasmonic waveguide. Opt. Express **20**, 25345–25355 (2012)
47. A. Gupta, D. Akin, R. Bashir, Detection of bacteria cells and antibodies using surface micromachined thin silicon cantilever resonators. J. Vac. Sci. Technol. B **22**, 2785–2791 (2004)
48. K.D. Vos et al., SOI optical microring resonator with poly (ethylene glycol) polymer brush for label-free biosensor applications. Biosens. Bioelectron. **24**, 2528–2533 (2009)
49. S. Ghosh, B.M.A. Rahman, An innovative straight resonator incorporating a vertical slot as an efficient bio-chemical sensor. IEEE J. Sel. Top. Quantum Electron. **23**, 132–139 (2017)
50. S.H. Yang et al., Giant birefringence in multi-slotted silicon nanophotonic waveguides. Opt. Express **16**, 8306–8316 (2008)
51. Sucrose Conversion Table, File code 135-A-50, United States Department of Agriculture (USDA) (1981)
52. B.M.A. Rahman, J.B. Davies, Analysis of optical waveguide discontinuities. J. Lightwave Technol. **6**, 52–57 (1988)
53. S.A. Kumar, S.M. Chen, Nanostructured zinc oxide particles in chemically modified electrodes for biosensor applications. Anal. Lett. **41**, 141–158 (2008)
54. Z.K. Tang et al., Room-temperature ultraviolet laser emission from self-assembled ZnO microcrystallite thin films. Appl. Phys. Lett. **72**, 3270–3272 (1998)
55. M. Law et al., Nanowire dye-sensitized solar cells. Nat. Mater. **4**, 455–459 (2005)
56. A. Janotti, C.G. Van de Walle, Fundamentals of zinc oxide as a semiconductor. Rep. Prog. Phys. **72**, 126501 (2009)
57. P.G. Etchegoin, E.C. Le Ru, M. Meyer, An analytic model for the optical properties of gold. J. Chem. Phys. **125**, 164705 (2006)
58. G.E. Jellison, L.A. Boatner, Optical functions of uniaxial ZnO determined by generalized ellipsometry. Phys. Rev. B **58**, 3586–3589 (1998)

59. J. Han et al., Optical and dielectric properties of ZnO tetrapod structures at terahertz frequencies. Appl. Phys. Lett. **89**, 031107 (2006)
60. Y. Chen, C.L. Zhu, G. Xiao, Reduced-temperature ethanol sensing characteristics of flower-like ZnO nanorods synthesized by a sonochemical method. Nanotechnology **17**, 4537 (2006)
61. N.T. Kejalakshmy, K.T.V. Grattan, B.M.A. Rahman, Investigation of the optical model properties of Al^{+3} doped ZnO-coated Au waveguide for gas sensing applications using the finite element method. IEEE Sens. J. **16**, 1176–1181 (2015)
62. L. Gas, Lower and upper explosive limits for flammable gases and vapors. Matheson Gas Products (2013)
63. S. Babar, J.H. Weaver, Optical constants of Cu, Ag and Au revisited. Appl. Opt. **54**, 477–481 (2015)
64. H.H. Li, Refractive index of silicon and germanium and its wavelength and temperature derivatives. J. Phys. Chem. Ref. Data **9**, 561–658 (1980)
65. W. Wang, Ethanol sensing properties of porous ZnO spheres via hydrothermal route. J. Mater. Sci. **48**, 3232–3238 (2013)
66. L. Zhang et al., Facile synthesis and ultrahigh ethanol response of hierarchically porous ZnO nanoplates. Sens. Actuators B Chem. **54**, 3–15 (1999)
67. Z. Jiang, J. Zhan, Fabrication and gas-sensing properties of porous-ZnO nanoplates. Adv. Mater. **161**, 209–215 (2012)
68. A. Garahan, L. Pilon, J. Yin et al., Effective optical properties of absorbing nanoporous and nanocomposite thin films. J Appl. Phys. **101**, Art no 014320 (2007)
69. W.L. Bond, Measurement of the refractive indices of several crystals. J. Appl. Phys. **36**, 1674–1677 (1965)
70. S. Ghosh, B.M.A. Rahman, A compact Mach-Zehnder interferometer using composite plasmonic waveguide for ethanol vapor sensing. J. Lightwave Technol. **35**, 3003–3011 (2017)